Assessing the limits of Rayleigh-Debye-Gans theory: Phasor analysis of a bisphere

Clément Argentin, Matthew Berg, Marek Mazur, Romain Ceolato, Jérôme Yon

▶ **To cite this version:**

Clément Argentin, Matthew Berg, Marek Mazur, Romain Ceolato, Jérôme Yon. Assessing the limits of Rayleigh-Debye-Gans theory: Phasor analysis of a bisphere. Journal of Quantitative Spectroscopy and Radiative Transfer, 2021, 264, pp.107550. 10.1016/j.jqsrt.2021.107550 . hal-03141094

HAL Id: hal-03141094

https://normandie-univ.hal.science/hal-03141094v1

Submitted on 9 Mar 2023

HAL is a multi-disciplinary open access archive for the deposit and dissemination of scientific research documents, whether they are published or not. The documents may come from teaching and research institutions in France or abroad, or from public or private research centers.

L'archive ouverte pluridisciplinaire **HAL**, est destinée au dépôt et à la diffusion de documents scientifiques de niveau recherche, publiés ou non, émanant des établissements d'enseignement et de recherche français ou étrangers, des laboratoires publics ou privés.

Distributed under a Creative Commons Attribution - NonCommercial 4.0 International License

Version of Record: https://www.sciencedirect.com/science/article/pii/S0022407321000431
Manuscript_c5170687ca4784391ff7e01117a82cfa

Assessing the limits of Rayleigh-Debye-Gans theory: Phasor analysis of a bisphere

Clément Argentin[a], Matthew J. Berg[b], Marek Mazur[a], Romain Ceolato[c], Jérôme Yon[a,*]

[a]*Normandie Univ, UNIROUEN, INSA Rouen, CNRS, CORIA, 76000 Rouen, France.*
[b]*Kansas State University, Department of Physics, 1228 N. 17th St., Manhattan, KS 66506-2601, USA*
[c]*ONERA, The French Aerospace Lab, Université de Toulouse, FR 31055, France*

Abstract

Rayleigh-Debye-Gans (RDG) theory is a commonly used approximation for light scattering and absorption by nanoparticles in the visible spectrum. The aim of this study is to advance our understanding for the origin of empirically observed deviations between accurate calculations of forward scattering and the absorption cross-sections and those predicted by RDG. For this purpose, we investigate the internal electric field within bi-spherical nanoparticles in several cases. The fixed-size constituent spheres of the bispheres are either separated or overlapped and are investigated using the discrete dipole approximation (DDA). To study the internal electric fields, we apply a phasor approach, which provides a semi-graphical way to understand the deviation of the forward scattering (A) and that of the absorption cross section (h) with respect to the RDG. The phasor approach reveals the influence of the bisphere orientation, absorption function $E(m)$, scattering function $F(m)$, and wavelength. It is observed that RDG tends to overestimate the forward scattering, i.e., $A < 1$, as well as absorption $h < 1$ for larger size parameters, and thus, shorter wavelength. At the opposite limit, a decreasing absorption function $E(m)$ leads to RDG underestimating the true scattered intensity. An explanation for this effect is a competition between the non-uniformity of the internal electric field and the phase shift of the phasors, leading to different results than those predicted by RDG and the amount of dipoles scattering in-phase.

Keywords: Bisphere, Rayleigh-Debye-Gans approximation, Internal coupling, Discrete dipole approximation, Phasor analysis, Scattering, Absorption

*Corresponding author.*E-mail address:* yon@coria.fr

© 2021 published by Elsevier. This manuscript is made available under the CC BY NC user license
https://creativecommons.org/licenses/by-nc/4.0/

Nomenclature

Manuscript symbols

λ	Wavelength	[m]
ρ	Phase shift parameter	
ϕ	Phase shift of the internal electric field relative to RDG	[°]
	Orientation state of the particle	
A	Forward scattering correction to RDG	
a	Particle radius	[m]
C^{abs}	Absorption cross section	[m^2]
C^{sca}	Scattering cross section	[m^2]
d	Dipole-dipole separation distance	[m]
$\mathrm{d}C^{\mathrm{sca}}/\mathrm{d}\Omega$	Differential scattering cross section	[m^2]
d_{ij}	Distance between sphere centers in a bisphere	[m]
$E(m)$	RDG absorption function	
$\mathbf{E}^{\mathrm{inc}}$	Incident electric field	[kg m s^{-3} A^{-1}]
$\mathbf{E}^{\mathrm{int}}$	Internal electric field	[kg m s^{-3} A^{-1}]
$\mathbf{E}^{\mathrm{int}}_{\mathrm{RDG}}$	RDG internal electric field	[kg m s^{-3} A^{-1}]
$\mathbf{E}^{\mathrm{sca}}$	Scattering electric field	[kg m s^{-3} A^{-1}]
$\mathbf{E}^{\mathrm{sca}}_1$	Far-field scattering amplitude	[kg m^2 s^{-3} A^{-1}]
$F(m)$	RDG scattering function	
h	Absorption correction to RDG	
k	Wave number	[m^{-1}]
$m = n + i\kappa$	Complex refractive index	
$\hat{\mathbf{n}}_{\mathrm{inc}}$	Unit vector in the direction of the incident wave	
$\mathbf{r}$	Vector from the origin to the detector: observation point	[m]
$\hat{\mathbf{r}}$	Unit vector in the direction of $\mathbf{r}$	
$\mathbf{r}_i$	Position of the i^{th} volume element	[m]
$\langle x \rangle$	Orientation average of x	
$\overline{x}$	Average of x over the particle volume	
x_{p}	Particle size parameter	

$z_{x,i},\ z_{y,i},\ z_{z,i}$	Phasors	
$[\cdots]_{\mathrm{hh}}$	Horizontal-horizontal polarization	
$[\cdots]_{\mathrm{vv}}$	Vertical-vertical polarization	
$[\cdots]_{\mathrm{v}}$	Vertical incident polarization	

Appendix symbols

μ_{o}	Magnetic permeability of free space	[m kg s^{-2} A^{-2}]
χ	Electric susceptibility	
$\mathbf{B}^{\mathrm{sca}}$	Scattered magnetic field	[kg s^{-2} A^{-1}]
I	Light intensity (irradiance)	[W m^{-2}]
$\overleftrightarrow{\mathbf{I}}$	Cartesian identity dyadic	
$\mathbf{P}_i$	Electric polarization of element i	[C m^{-2}]
$\hat{\mathbf{r}} \otimes \hat{\mathbf{r}}$	Dyadic product of vectors $\hat{\mathbf{r}}$ and $\hat{\mathbf{r}}$	
$\mathbf{S}$	Poynting vector	[W m^{-2}]

Highlights

- RDG limits are explored for an overlapped bisphere.
- Forward scattering and absorption corrections are related to the internal electric field non-uniformity.
- Optical index, orientation and wavelength dependencies are investigated.
- The coupling between the spheres is limited to two sphere diameters of distance.
- Sharp curvatures produce large gradients of the electric field, and thus, RDG deviations.

1. Introduction

Nanometer sized aerosol particles and colloids are generated intentionally in certain industrial processes [1] or unintentionally and without control, e.g., from vehicular activity and polymer combustion [2, 3]. Due to their small size and thermal agitation, these particles are often encountered in aggregated form. Different techniques exist to analyse the emission or generation of these particles, with light scattering methods being a particularly effective technique. Indeed, light-scattering techniques enable an affordable and *in-situ* diagnostic method with the possibility of high spatial and temporal resolution. A common challenge for light scattering studies of aerosols is how to best interpret the data to retrieve particle properties of interest. For this purpose, fast and efficient methods based on simplified models for scattering are used. Rayleigh scattering is one example, involving a simple formulation, but it is limited to particles with small size parameter $x_\mathrm{p} = ka \ll 1$ where $k = 2\pi/\lambda$, λ is the (vacuum) wavelength, and a is the particle radius.

Rayleigh Debye Gans (RDG) theory is another approximation for light scattering for particles that is based on the Rayleigh approximation and is applicable to non-spherical objects. In addition to the constraint on the size parameter, the particle has to be nearly transparent, i.e., $|m-1| \ll 1$, where $m = n+i\kappa$ is the wavelength-dependent complex-valued refractive index and the related phase shift parameter $\rho = 2x_\mathrm{p}|m-1|$ should also be $\rho < 1$. Under these conditions, the absorption-cross section is $C^\mathrm{abs} = 6\pi V E(m)/\lambda$ where V is the particle volume and

$$E(m) = \mathrm{Im}\left\{\frac{m^2-1}{m^2+2}\right\} \tag{1}$$

is the absorption function [4]. Similarly, the forward-scattering differential cross-section for vertically polarized incident light and scattered light polarized in the same direction is [4]

$$\frac{\mathrm{d}C^\mathrm{sca}_\mathrm{vv}}{\mathrm{d}\Omega}(\theta = 0^\circ) = \frac{9\pi^2 V^2}{\lambda^4} F(m) \tag{2}$$

where the scattering function is

$$F(m) = \left|\frac{m^2-1}{m^2+2}\right|^2. \tag{3}$$

At other scattering angles θ, scattered light originating from different regions in a particle can interfere, which reduces the overall scattering intensity. This effect depends on the particle

size and shape [5]. In that case, Eq. (2) is modulated by a function called the structure factor. A frequently encountered case where such a description for angular scattering is used is for fractal aggregates where the approximation is called RDG for Fractal Aggregates (RDG-FA). The approximation is typically applied to fractal aggregates of spherical primary particles, or monomers, of soot nanoparticles and is extensively described in the literature, e.g., see [6]. At the monomer scale, the RDG approximation assumes the electric field is uniform within the monomer based given that $a \ll \lambda$. The interference diminishing the scattered intensity as described by the structure factor then originates from the differing position of the many monomers composing an aggregate.

Most formulations for the structure factor rely on the hypothesis that each volume element in a monomer particle "sees," and then scatters, only the incident light. That is, scattering from the monomer is envisioned as each volume element responding to the incident field ignoring any perturbation caused by scattering from the other elements in the particle. This simplification is refereed to as "no internal coupling" or as the "absence of multiple scattering," and its utility is to greatly simplify the mathematical description of scattering from the entire aggregate. Formally, this simplification is only justified for $m \to 1$, i.e., when refraction effects are negligible. Yet, in many applications m can be large, and often features a significant imaginary part describing absorption, and internal coupling is not negligible leading to substantial disagreement between the true angular-scattering and that predicted by RDG-FA.

A number of studies investigate and quantify the error made by invoking the RDG approximation. For fractal aggregates in particular, Farias et al. [7] show that the RDG-FA is a reasonable approximation to within 10% error if $x_\mathrm{p} \leq 0.3$. Nevertheless, it seems that theory is not suitable for particular aggregates as super-aggregates Ceolato et al. [8]. More recently, the error is studied in terms of correction factors A and h, which bring the RDG-FA approximately into agreement with the true forward-scattering (A) and absorption cross section (h) behavior of aggregates. Liu and Smallwood [9] quantify the error of the RDG-FA approximation focusing on absorption, h, and vary the number of monomers in the aggregate as well as the wavelength, concluding an error $h \leq 10\%$. Dependence of the correction factors with a number of parameters are described in other work, including the effect of the

monomer number [10], wavelength [11], monomer overlapping and necking [12], coating [13], monomer polydispersity [14] and finally m [15]. These studies show a strong impact of those parameters on the correction factors A and h. Indeed, RDG can overestimate or underestimate the cross-sections by more than 40% at shorter wavelengths and by 10% at longer wavelengths. Kelesidis et al. [16] recently report an underestimation reaching 50%. In some of the studies mentioned, an empirical relationship between A and h is reported, namely $h = 1.11A$, which has yet to be justified theoretically.

Unfortunately, despite the amount work dedicated to the topic of the RDG approximation's validity, the correction factors A and h do not yield simple and universally applicable analytical expressions useful to improve the precision of scattering-measurement interpretation. The explanation relies on the complicated interactions of electromagnetic coupling within and among monomers, which continue to limit our understanding for the scattering phenomenon even for such small-scale particles. It is therefore justified to take a fresh look at the problem and apply new tools. In this paper, the RDG correction is examined for nanoparticles by studying the internal electric field within the particles. Indeed, contrary to the basic assumption of the RDG approximation – that the internal field in a monomer is uniform – complex structures such as aggregates are known to exhibit significantly different amplitudes of the internal electric field from one monomer to another. The new tool applied here is that of phasor analysis introduced by Berg [17, 18]. Here, the phasor is a complex number representing the contribution to the far-field scattered field due to the local internal field at a volume element in a particles. The analysis is useful because it can provides, in some cases, a semi-graphical way to understand how the particle's morphology affects it scattering behavior. An example is the explanation in [19] for why orientational averaging is critical to find approximate agreement between RDG and and the exact scattering for soot fractal aggregates.

In this study, phasor analysis is adapted to quantify how each volume element in a particle contributes to departures of the true scattering from the RDG prediction. Slices through the particles are visualized and examined to reveal which parts of the particles cause under- or over-estimation of the scattering relative to RDG. This novel approach is applied to the study of the electromagnetic coupling between two equal-sized spherical monomers since

they are the simplest case representing "multiple scattering" in an aggregate. Specifically, we focus on monomers that are (i) separated, (ii) in point contact, or (iii) overlapping. The influence of λ and m are investigated. The analysis is carried out using the Lorentz-Lorenz factor, i.e., $E(m)$ and $F(m)$, which represent, respectively, the absorption and scattering efficiency of a particle in RDG theory. This work contrasts [15] where the influence of the real part n and imaginary part κ of the refractive index m is investigated.

After presentation of the numerical setup, the correction to RDG for forward scattering is first presented for the bisphere configurations. Then, the phasor analysis is presented to explain the observed trends of that correction. Finally, the internal electric field is interpreted as a local contribution to the correction to bring to RDG respectively for forward scattering A and for absorption h.

2. Numerical Setup

Because the aim is to investigate overlapped spheres, among other considerations, the discrete dipole approximation (DDA) model [20–22] is used rather than T-matrix [23], which has difficulty with such particles. The DDA is a general method to compute the scattering and absorption of electromagnetic waves by particles of arbitrary geometry and composition. The main approximation in the DDA is that the particle is represented by a collection of discrete coupled electric-dipoles that reside on a cubic lattice spanning the particle volume. In other words, the DDA formulation can be interpreted as replacing a particle by a set of interacting dipoles. The accuracy of DDA is thus determined by the fineness of this lattice and many well-validated public codes are available; we choose that of Drain here [24] called DDSCAT. More precisely, the module "N SPHERES" in DDSCAT is used to generate a pair of spherical particles. The code provides the internal electric field, which is then post-processed for the phasor analysis with an in-house Python code.

We consider two spherical particles, i.e., a bisphere, where the radius of each sphere is fixed at $a = 21.1\,\text{nm}$ and separation distance d_{ij} with respect to each sphere's center, i and j, varies, see Fig.1. The incident light is a linearly polarized plane wave that propagates along the x-axis and is polarized along the y-axis. The majority of the computations below are performed with $\lambda = 532\,\text{nm}$ except for the study of the wavelength dependence. A large

range for m is explored and a constant dipole-dipole separation of $d = 1.77\,\text{nm}$ is used to fulfill the DDA accuracy criteria according to Draine et al.[24], which is $|m|kd < 0.5$ (see Appendix A) and $|m-1| < 2$. We used a value of $d = 0.44\,\text{nm}$ in the figures (Figs. 6, 7 and E.11), where cross-sectional views through the bisphere are shown to display the internal-field behaviour with an higher resolution. Because the criteria of Draine et al. is already satisfied, those more refined cases remain valid and the corresponding average quantities are not affected (see Appendix B). The internal fields are calculated for 400 isotropically distributed orientations of the bisphere. We find that such a distribution is sufficient to simulate a randomly oriented mirror-symmetric particle the bisphere here [25].

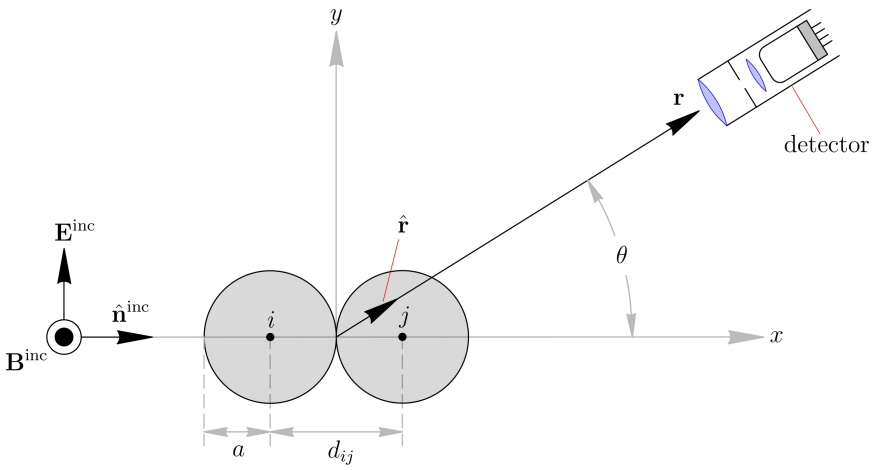

Figure 1: Scattering arrangement consisting of two identical spherical monomers illuminated by a linearly polarized plane wave. The wave propagates along the x-axis, $\hat{\mathbf{n}}^{\text{inc}} = \hat{\mathbf{x}}$, and is polarized along the y-axis, i.e., $\hat{\mathbf{E}}^{\text{inc}}$, with the origin at the geometric center of the particle arrangement. Each particle has radius a and center-to-center separation d_{ij}. The detector at $\mathbf{r}$ resides in the horizontal x-z scattering plane and $\mathbf{r}$ resides in the particle's far-field zone as defined by [26].

It is shown in [22] that the DDA can be derived from the volume integral equation (VIE), which is a solution to the Maxwell wave equation describing scattering from any particle. The VIE can be discretized in a manner suitable for phasor analysis as follows. First, we consider a linearly polarized plane wave incident on a bisphere with electric field given by

$$\mathbf{E}^{\text{inc}}(\mathbf{r}) = \mathbf{E}_{\text{o}}^{\text{inc}} \exp(ik\hat{\mathbf{n}}^{\text{inc}} \cdot \mathbf{r}) \tag{4}$$

where the polarization is taken along the y-axis, i.e., $\mathbf{E}_{\text{o}}^{\text{inc}} = E_{\text{o}}\hat{\mathbf{y}}$ with E_{o} being real-valued for simplicity, and the propagation direction is along the x-axis, i.e., $\hat{\mathbf{n}}^{\text{inc}} = \hat{\mathbf{x}}$. Next, we consider

a well-collimated detector located at an observation point $\mathbf{r}$ that is confined to the x-z plane and is restricted to the particle's far-field zone. The meaning of a well collimated detector is described in [27], but for the purposes here can be assumed to measure the intensity of the scattered wave. In such a case, the scattered wave is also polarized along the y-axis for a symmetric particle like the bisphere, see Appendix C for further explanation. In other words, we are describing the vertical-vertical polarization configuration between incident and scattered light and will denote this by the subscript "vv." Next, a scattering amplitude $\mathbf{E}^{\text{sca}}_{1,\text{vv}}$ is isolated from the simplified VIE as

$$\mathbf{E}^{\text{sca}}_{1,\text{vv}}(\hat{\mathbf{r}}) = \hat{\mathbf{y}}\frac{3k^2}{4\pi}\frac{m^2-1}{m^2+2}E_\text{o}\int_V \frac{m^2+2}{3E_\text{o}}E^{\text{int}}_y(\mathbf{r}')\exp(-ik\hat{\mathbf{r}}\cdot\mathbf{r}')dV'. \tag{5}$$

Note that the actual scattered field $\mathbf{E}^{\text{sca}}(\mathbf{r})$ involves multiplication of Eq. (5) by the spherical wave term $\exp(ikr)/r$ as explained in Appendix C. The significance of $\mathbf{E}^{\text{sca}}_{1,\text{vv}}$ is that it describes the angular dependence $\hat{\mathbf{r}}$ of the scattered light independent of the distance from the particle r. Finally, the integral in Eq. (5) is discretized into N small cubical volume elements ΔV such that the particle volume $V = N\Delta V$, which gives

$$\mathbf{E}^{\text{sca}}_{1,\text{vv}}(\hat{\mathbf{r}}) = \hat{\mathbf{y}}\frac{3k^2}{4\pi}\frac{m^2-1}{m^2+2}E_\text{o}\sum_{i=1}^{N} z_{y,i}(\hat{\mathbf{r}})\,\Delta V, \tag{6}$$

where the phasors $z_{y,i}$ are given by

$$z_{y,i}(\hat{\mathbf{r}}) = \frac{m^2+2}{3E_\text{o}}E^{\text{int}}_y(\mathbf{r}_i)\exp(-ik\hat{\mathbf{r}}\cdot\mathbf{r}_i). \tag{7}$$

In Eq. (7), $\mathbf{r}_i$ is the location of a volume element in the particle, $\mathbf{E}^{\text{int}}$ is assumed uniform in a given ΔV, and the sum in Eq. (6) runs over all N volume elements. We note for later use below, that when Eq. (6) is evaluated in the forward-scattering direction, $\hat{\mathbf{r}} = \hat{\mathbf{n}}^{\text{inc}} = \hat{\mathbf{x}}$, the phasors in Eq. (7) simplify to

$$z_{y,i}(\hat{\mathbf{x}}) = \frac{m^2+2}{3E_\text{o}}E^{\text{int}}_y(\mathbf{r}_i)\exp(-ikx'_i), \tag{8}$$

where x'_i is the x-component of the $\mathbf{r}_i$ volume element.

The physical interpretation of Eq. (6) is that the scattered electric field at the detector can be though of as the superposition of many spherical waves, or wavelets, with complex-valued amplitudes given by the phasors $z_{y,i}$, that are radiated from each volume element

in the particle depending on the locally defined internal electric field $\mathbf{E}^{\text{int}}$. The wavelets interfere due to magnitude and phase shifts caused by variations in $\mathbf{E}^{\text{int}}$ from one $\mathbf{r}_i$ to another, the different locations of the volume elements themselves, and the direction to the detector. In other words, Eq. (6) can be thought of as Huygens' principle, except with the complete vector nature of the electromagnetic wave taken into account and no approximation other than the discretization of the integral in Eq. (6). Being simply complex numbers, the phasors can be graphically presented in a polar plot, which gives access to the contribution of each volume element as the direction $\hat{\mathbf{r}}$ varies; this is the gist of phasor analysis [17]. In the following, we use phasor analysis to identify and understand the deviations from the RDG theory in Sec. 3.2 by linking the phasors with the correction term A_{vv} and h_{v}. Before doing so, however, a preliminary investigation will show the circumstances under which such deviations occur for a bispere considering different m and d_{ij}. The results will be used to predict the possible behaviours and outcomes of the in subsequent phasor analysis.

3. Results

3.1. RDG correction to forward scattering: A global approach

Figure 2(a) and Fig. 2(b) report the forward scattering RDG correction A for two spheres of size parameter is $ka = 0.249$ as a function of d_{ij} from being overlapped with $d_{ij}/2a \leq 1$, in point contact for $d_{ij}/2a = 1$, and separated for $d_{ij}/2a > 1$. The symbols corresponds to different values of m. In Fig. 2(a), the scattering function is fixed at $F(m) = 0.3$ and absorption function $E(m)$ is varied. In Fig.2(b), the absorption function is fixed at $E(m) = 0.3$ while $F(m)$ varies. The data reported in these plots include bars to indicate the standard variation for the individual orientations orientation averaging.

Notice in Fig. 2(a) and Fig. 2(b) that deviation of the forward scattering compared to RDG can be observed even for an isolated sphere, $d_{ij}/2a = 0$. The deviation does not exceed 1.07 in this figure indicating a relatively low underprediction of RDG for a single sphere, which is explained by the small size parameter $ka = 0.249$. Also, the standard deviation in Fig. 2(a) and Fig. 2(b) is zero since an isolated sphere is perfectly isotropic. Yet, the fact the $m \neq 1$ seems to have a strong influence on correction A as detailed in Fig. 2(c). Indeed, larger corrections are favored by a high scattering function $F(m)$ and a low absorption function

$E(m)$. This result is in agreement with Sorensen's study [15], which shows an increase of A the real part of the refractive index n and a decrease with increasing imaginary part κ. Nevertheless, when represented as a function of n and κ, as reported in Appendix D, the influence of κ seems to be weaker than that of n. The results in Fig. 2(a) and 2(b) display a similar influence of $E(m)$ and $F(m)$ on A. Figure 2(c) shows a general under-prediction of RDG for an isolated sphere that is small compared to the wavelength since A is bounded in the range $[\approx 1 - 1.16]$. Next we will show that increasing the absorption function $E(m)$ also increases the homogeneity of the internal electric field in the bisphere.

Increasing the distance d_{ij} for an overlapping bisphere shows that the correction factor A is linearly increased or linearly decreased depending on the value of m as seen in Fig. 2. The maximum deviation to the correction regarding the one for the isolated sphere is reached for $d_{ij}/2a \approx 0.8$ (corresponding to an overlapping coefficient of 0.2). It is interesting to notice that this level of overlap is often observed for flame-generated soot [28, 29]. The range of A is larger for this distance than for isolated spheres (RDG correction more important for a bisphere) but the hierarchy related to the optical index is similar. Indeed, the corresponding dependence to the optical index is reported in Fig. 2(d) showing a similar trend compared to Fig. 2(c). One can also observe an increase of the bars amplitude indicating an increasing dispersion by increasing $d_{ij}/2a$ up to 0.8 related to the particle orientation, which is explained by an increase of the particle anisotropy.

For $d_{ij}/2a > 0.8$, the deviation of the correction factor from $A = 1$ decreases along with the standard deviation bars. The deviation follows an exponential decay, or increase, with d_{ij} depending on the value for m as shown by the dashed lines in Fig. 2(a) and Fig. 2(b). Notice that the trends appear to converge to an asymptotic value that is corresponds A for an isolated sphere, i.e., when $d_{ij} = 0$. Several interpretations can be formed from these observations. First, the RDG approximation performs well, $< 10\%$ error, if the component spheres of the bisphere are separated by $d_{ij}/2a \gtrsim 2$. This short coupling-distance is observed by [30] where similar ranges are reported for larger metallic spheres. Second, the asymptotic behavior implies that electromagnetic coupling between the component sphere does not appear to affect the internal field experienced by each spheres when treated in the independent scattering approximation. It is interesting to note the relative small-size of the standard de-

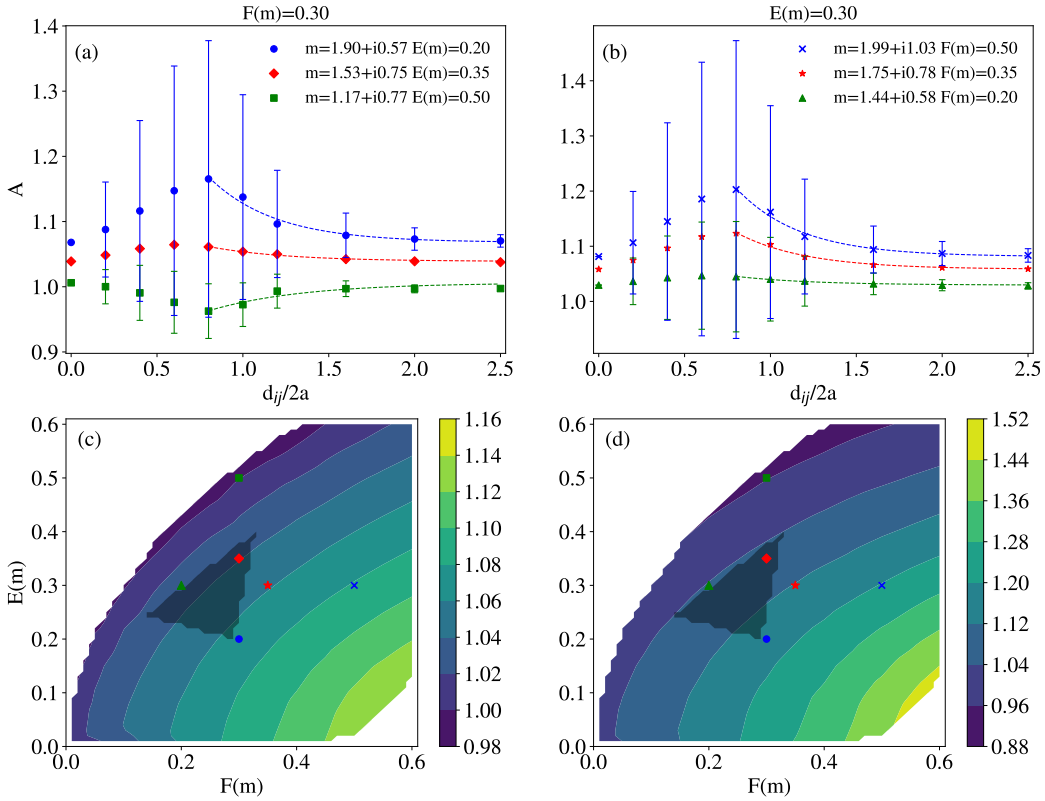

Figure 2: Evolution of forward scattering correction to RDG, A, for a bisphere. Plots (a) and (b) show A as a function of the bisphere's center-to-center separation d_{ij} normalized by the sphere diameter $2a$ where m is changed to keep $F(m)$ or $E(m)$ constant, respectively. Plot (c) shows the dependence of A as a function of m for a single sphere ($d_{ij} = 0$) with $ka = 0.249$ and (d) shows the same for an overlapping bisphere with $d_{ij}/2a > 0.8$ which provided the maximum amplitudes for A in plot (a) and (b). In plot (c) and (d), the symbols indicate the $F(m)$ and $E(m)$ values for the refractive indexes considered in plots (a) and (b). The black triangle in plot (c) and (d) corresponds to the domain related to soot material, delimited by organic, graphitic, and amorphous compositions at $\lambda = 532$ nm (see Table 1 in [15]).

viation bars as d_{ij} increases while also noting that the anisotropy of the separated-bisphere particle is increasing with d_{ij}.

The present global analysis highlights that the dependence of A on the orientation of the particle is characterised by a balance between anisotropy and electromagnetic coupling itself, favored for larger $F(m)$ and lower $E(m)$. This study covers a large domain of $E(m)$ and $F(m)$, larger than one related to soot particles (represented by the dark triangles in Fig. 2(c) and Fig. 2(d)) which is the intended application of this study and for which the magnitude of the correction is reduced. The following section aims at going one step further and explaining the influence of the particle orientation on the amplitude of A by using the phasor representation.

3.2. RDG correction to forward scattering: Phasor representation

We now apply the phasor analysis of Berg [17] in an effort to understand the influence of particle morphology and m on the deviation of the forward-scattering differential cross-section from that given by the RDG approximation. A phasor $z_{y,i}$ is as a complex number associated with the volume element at $\mathbf{r}_i$ in the particle. The summation of all phasors for the entire particle volume V is proportional to the far-field scattering amplitude $\mathbf{E}^{\mathrm{sca}}_{1,\mathrm{vv}}$ as given by Eq.6. Each phasor itself is proportional to the internal electric field $\mathbf{E}^{\mathrm{int}}_{y}$ within its volume element and depends on $\mathbf{r}_i$ and direction $\hat{\mathbf{r}}$ to the detector, i.e., the scattering angle, as shown by Eq. (7). These dependencies lead to constructive or destructive interference between the wavelets described by the phasors, recall Sec. 2.

The phasor as defined here, Eq. (7), is proportional to that used in Berg [17] but is modified in order to analytically express the deviation from RDG theory. Further explanation is given in Appendix C, but we note that the correction to the RDG forward-scattering for the vertical-vertical scattering configuration when the orientation of the bisphere is given by ψ can be expressed as

$$A_{\mathrm{vv}}(\psi) = \frac{\dfrac{\mathrm{d}C^{\mathrm{sca}}_{\mathrm{vv}}}{\mathrm{d}\Omega}(0^\circ)}{\dfrac{\mathrm{d}C^{\mathrm{sca}}_{\mathrm{RDG,vv}}}{d\Omega}(0^\circ)} = |\overline{z_{y,i}}|^2\,, \tag{9}$$

where the phasors are given by Eq. (8). The overbar in Eq. (9) denotes spatial averaging of the phasors over V, see Eq. (F.5), and the vertical bars denote absolute value. For a spherical

particle $A_{\mathrm{vv}} = A_{\mathrm{hh}}$ where hh denotes the horizontal-horizontal polarization configuration for scattering. We note that the A investigated in Yon et al. [11], Sorensen et al. [15] as well as in section 3.1 corresponds to the orientation averaging of A_{vv} i.e by considering different ψ. After orientation averaging $A = \langle A_{\mathrm{vv}} \rangle = \langle A_{\mathrm{hh}} \rangle$, where the brackets represent the orientation averaging.

In the RDG approximation for a particle with $a \ll \lambda$, the internal electric field is uniform and proportional to the incident field Eq. (4) as [31]:

$$\mathbf{E}^{\mathrm{int}}_{\mathrm{RDG}}(\mathbf{r}) = \left(\frac{3}{m^2 + 2} \right) \mathbf{E}^{\mathrm{inc}}(\mathbf{r}). \tag{10}$$

When Eq. (10) holds, the phasors in Eq. (8) simplify to $z_{\mathrm{RDG}} = 1 + 0i$ for the forward direction $\hat{\mathbf{r}} = \hat{\mathbf{n}}^{\mathrm{inc}}$, and consequently via Eq. (9), $A = 1$ meaning that no correction is necessary. Physically, this corresponds to all of the wavelets of the particle radiating to $\mathbf{r}$ in phase. To compare the true forward scattering to this approximation with phasor analysis in the following, the DDA of Sec. 2 is used to calculate the internal field needed in Eq. (8).

A phasor plot is a polar plot where the horizontal and vertical axes represent, respectively, the real part and imaginary part of the phasor. Figure 3 presents three phasor plots corresponding to an isolated sphere and two overlapped spheres (a bisphere) with $d_{ij}/2a = 0.8$ and with different orientations. The phasors are represented by green points. One can see that a dispersion of the phasor points exists around the theoretical value expected for the RDG approximation, i.e., $z_{\mathrm{RDG}} = 1 + 0i$, even for the isolated sphere in Fig. 3(a). Nevertheless, the corresponding mean spatial averaging (large yellow point) is located close to the RDG value. Since A is the square of the modulus of the mean phasor, Eq. (9), this means that the correction to the RDG prediction is close to 1. The dispersion of the phasors in Fig. 3(a) is caused by a non-uniformity of the internal electric field. Yet, the character of the non-uniformity appear to such that a sufficient degree of partial cancellations of the phasors in the mean yield a result approximately consistent with RDG. This conclusion also holds for the horizontally oriented bisphere in Fig. 3(b) although to a lesser degree. In Fig. 3(c) where a vertically oriented bisphere is considered, the phasors are dispersed to a greater extent. In particular, the dispersion is shifted outside of the disc of modulus 1 (the semicircle shown) producing an average phasor modulus greater than 1 and a corresponding correction

to the RDG of $A_{\rm vv}(\psi) = 1.072$ (in the orientation configuration of plot c). Compare this to $A_{\rm vv}(\psi) = 0.923$ for the horizontally oriented bisphere in Fig. 3(b). In conclusion, the phasor dispersion for the bisphere can be similar to or much greater than the dispersion for an isolated sphere depending on the bisphere orientation. The different dispersion produce different values for the average phasor modulus, and thus, the RDG approximation.

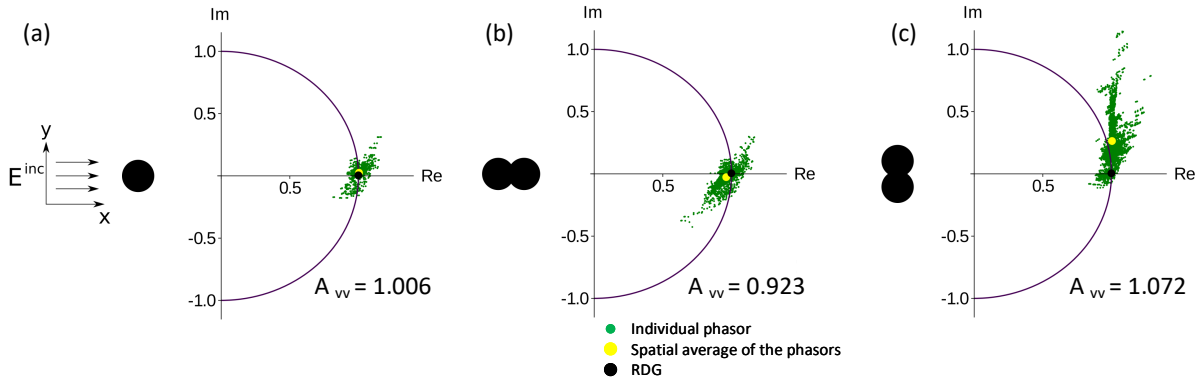

Figure 3: Phasor plots for an isolated sphere (a), and a bisphere with overlapping component spheres where $d_{ij}/2a = 0.8$ in (b) and (c). The orientation of the bisphere is shown relative to the propagation direction of the incident wave, i.e., $\hat{\mathbf{n}}^{\rm inc} = \hat{\mathbf{x}}$. The size parameter for the isolated sphere, which is the same as the component sphere forming the bisphere, is $ka = 0.249$ and the refractive index for all is $m = 1.17 + 0.77i$. For comparison, the sphere-volume equivalent size parameter for the bisphere is $ka_{\rm ve} = 0.314$. Note that the polarization of the incident wave, Eq. (4) is directed along the y-axis and parallel to the symmetry axis of the bisphere in (c).

The orientation dependence of the phasors is examined further in Fig. 4. In Fig. 4(a) the spatially averaged phasors $\overline{z_{y,i}}$ for different orientations of a bisphere are shown by the open symbols for the value of $E(m)$ indicated as the bisphere changes orientation from horizontal to vertical. The horizontal and vertical bisphere-orientations are, respectively, at the beginning (bottom left corner) and at the end (top right corner) of the empty-symbol point groups for a given absorption function $E(m)$ and are shown for the $E(m) = 0.50$ case by the gray figures. The bisphere orientations are relative to $\hat{\mathbf{n}}^{\rm inc}$. The unity modulus is shown in Fig. 4(a) as the solid black line, which reveals that for some bisphere orientations (plot b), $|\overline{z_{y,i}}| < 1$, i.e., $A_{{\rm vv}(\psi)} < 1$, while for most other orientations $A_{\rm vv} > 1$. Remember that the RDG forward scattering is represented by the black point, $z_{\rm RDG} = 1 + 0i$. The filled

symbols in Fig. 4(a) show the phasors for a given $E(m)$ after averaging over all orientations, $\langle\overline{z_{y,i}}\rangle$ ($\langle\overline{z_{y,i}}\rangle|^2 \neq \langle|\overline{z_{y,i}}|^2\rangle = \langle A_{\rm vv}(\psi)\rangle$). Here, we see by looking at each $|\overline{z_{y,i}}(\psi)|$ that A can be less than one, indicating that RDG overpredicts the forward scattering, in the case that $E(m) = 0.50$, (green symbols). For the smaller values of the absorption function, namely $E(m) = 0.20$ (blue) and $E(m) = 0.35$ (red), we see that A increases to values larger than one, indicating that RDG underpredicts the forward scattering. The overall dispersion of the empty symbols increases in extent as the value of $E(m)$ decreases, which agrees with the behavior of the standard-deviation bars in Fig. 2(a) and Fig. 2(b). We can thus conclude that the less the material's absorption, the more the bisphere phasors disperse showing a stronger orientation-dependence of the non-uniformity of the internal electric field. In other words, increasing absorption of the material tends to enhance the uniformity of the internal electric field, and thus, will decrease the correction A needed to bring to RDG into agreement with the true forward scattering (see Appendix E).

Another feature of Fig. 4(a) is that for each $E(m)$ considered, the phasors disperse in the complex plane in a line-like pattern as the bisphere orientation evolves from horizontal to vertical. Moreover, the three phasor-pattern lines intersect not so far from $\overline{z_{y,i}} \approx 0.96 + 0i$, which is close, but not equal, to the RDG approximation at $z_{\rm RDG} = 1 + 0i$. The shift observed of this intersection point from $z_{\rm RDG}$ is dominated by the exponential term in the phasor definition, i.e., Eq. (8). This exponential is dominated by the size parameter of the particle, and thus, expresses the deviation of the true forward scattering from RDG as due to the condition $x_{\rm p} \ll 1$ being violated. The refractive index m, however, affects the slope of the phasor-pattern lines. This indicates that for a given material, on average, a constant phase-shift of the internal electric field relative to that predicted by RDG, i.e., Eq. (10), is observed for all bisphere orientations. Figure 4(b) shows this phase shift ϕ for different m in terms of $F(m)$ and $E(m)$. We observe that ϕ is small when $E(m)$ is small, in agreement with Fig. 4(a) and in accord with the second hypothesis of the RDG approximation that $\rho = 2x_{\rm p}|m-1| < 1$. As mentioned, increasing $E(m)$ result in the internal electric field becoming more uniform, and hence more in accordance with RDG, but the field phase will depart from that predicted by RDG. Indeed, we see in Fig. 4(b) that ϕ can reach 90° for the largest $E(m)$ and $F(m)$ considered. However, as can be seen for the soot particles

(dark triangle domain), the phase is restricted in a range covering 30° to 60°, which globally corresponds to straight lines between $E(m) = 0.20$ and $E(m) = 0.35$ in Fig. 4(a).

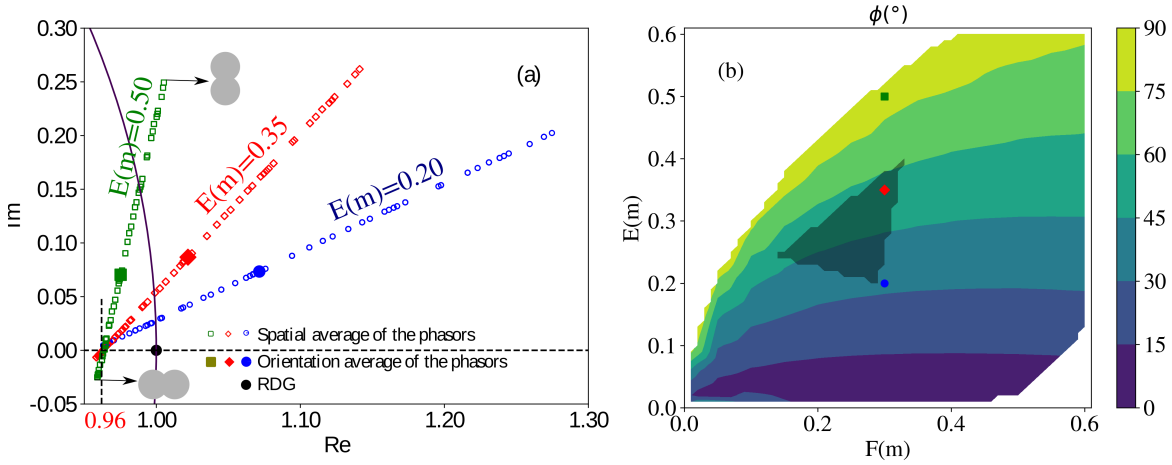

Figure 4: Effects of orientation ψ and refractive index m in phasor analysis. Plot (a) shows the spatially averaged phasors $\overline{z_{y,i}}$ (open symbols) for different orientations of an overlapped-sphere bisphere particle with $d_{ij}/2a = 0.8$. The pair of vertical or horizontally aligned gray disks indicate the bispheres' orientation with respect to $\hat{\mathbf{n}}^{\text{inc}}$. Three different refractive indices having the same scattering function $F(m) = 0.30$ but different absorption functions $E(m)$ are considered in (a): $E(m) = 0.50$ with $m = 1.17 + i0.77$ for the green points, $E(m) = 0.35$ with $m = 1.53 + i0.75$ for the red points, and $E(m) = 0.20$ with $m = 1.90 + i0.57$ for the blue points. The filled symbols in (a) correspond to the orientation average of all the phasors $\langle\overline{z_{y,i}}\rangle$. Plot (b) shows the phase-shift angle ϕ in degrees of the internal electric field relative to the RDG internal field, Eq. (10). Note that ϕ is also the slope of the phasor-pattern lines, open points, in the complex plane in plot (a). The black triangle in plot (c) ans (d) corresponds to the domain related to soot material, délimited by organic, graphitic, and amorphous compositions at $\lambda = 532$ nm (see Table 1 in [15]).

Similarly to Fig. 4(a), Fig. 5 illustrates the impact of the wavelength for a certain range of λ on the phasor distributions for the same bisphere as in Fig. 4(a) with a fixed refractive index $m = 1.17 + 0.77i$. The chosen range of wavelength is motivated by the conventional laser based techniques used for the characterization of soot particles, covering the visible domain. To begin, we consider once again the spatially averaged phasors $\overline{z_{y,i}}$, open symbols, as the bisphere evolves in orientation (varying Ψ isotropically). Solid symbols represent the orientation average of the phasors, $\langle\overline{z_{y,i}}\rangle$. Once more, we find that the phasors form a quasi-linear pattern in the complex plane as the orientation changes, but the slope and position of the pattern changes with λ. Notice that the overall length of the linear patterns

appear little affected by changing λ, in contrast to the effect due to the changes in m as shown in Fig. 4(a). The alignment of the (linear) phasor patterns is globally conserved but the phase angle is affected. Decreasing λ increases x_{p} and produces a horizontal shift of a phasor pattern towards the imaginary axis of the complex plane. This effect is driven by the exponential term in Eq. (8). In contrast to what happens when m changes, different λ cause a vertical shift of a phasor-pattern line, which can be explained by an increase of the the imaginary part of the internal field. Despite intricacies of the phasor distributions, we see that when orientationally averaged (filled symbols), the results show that an approximate value of $|\langle\overline{z_{y,i}}\rangle|^2 = 0.963 \pm 0.004$ holds for the wavelengths $\lambda = 442\,\mathrm{nm} - 1064\,\mathrm{nm}$. The corresponding value for A is indicated by the red dashed semi-circle. The departure to this value for $\lambda = 266\,\mathrm{nm}$ is about 7%. Finally, we note that because this analysis holds m fixed as λ varies, we are ignoring the spectral dispersion that must otherwise be taken into account. That is, our intent above is to understand how the parameters a, λ, m, and the bisphere orientation affect the phasor distributions rather than applying the analysis to a specific material. The wavelength has a strong effect on the phasor's horizontal shift as well as in the phase shift (slope) but, the mean value is relatively robust (0.963) for a wide range of λ. In comparison, by varying m, strong variations are been noticed.

In conclusion, the required correction to RDG for the forward scattering (A) due to dipolar coupling effects results from the combination of different effects. First, the electric field non uniformity depends on the orientation. Indeed, lowers $E(m)$ will increase the dispersion of the phasors in the polar plot. Second, the optical index and wavelength clearly impact the electric phase and thus also slope of the observed lines. Third, the intersection of the lines with the x axis can be shifted due to the increase of the size parameter. This effect explains the appearance of $A < 1$ (average phasor inside the polar plot). Hence larger A occurs for smaller $E(m)$ and smaller particles compared to the wavelength. Contrarily, lower A is obtained for large size parameters and larger $E(m)$. The wavelength seems to have a lower impact compared to the optical index, since phasor dispersion is less affected. The same conclusion can be extended to the effect of particle radius. Indeed, as shown by Mishchenko [32] when introducing the Scale Invariance Rule (SIR), the dimensionless scattering characteristics of an object is not changed if size parameter $x_p = ka$ is kept constant nor the

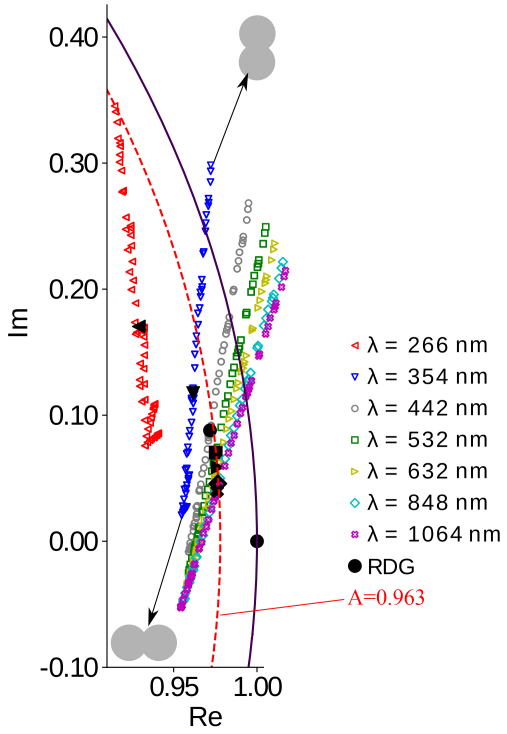

Figure 5: Phasor plot for spatially averaged phasors $\overline{z_{y,i}}$, open symbols, for different orientations of a bisphere with $d_{ij}/2a = 0.8$ and different wavelengths λ. The bisphere is the same as in Fig. 4 and the refractive index is $m = 1.17 + 0.77i$ corresponding to $E(m) = 0.50$ and $F(m) = 0.30$. Black filled symbols correspond to the orientation averaged phasor $\langle\overline{z_{y,i}}\rangle$ and the red dashed semi-circle the phasor where $|\langle\overline{z_{y,i}}\rangle|$ give a value $A = 0.963$.

correction factors to bring to RDG theory. Concretely, based on the provided results, for a wavelength $\lambda = 532$nm, the correction factors can be determined for a between 10 and 40nm.

3.3. RDG correction to the forward scattering: Spatial description

The previous sections show that the largest corrections to bring to RDG theory into agreement with the true forward-scattering are mainly due to the spatial non-uniformity of the internal electric field, which strongly depends on the bisphere orientation. This section aims to determine where non-uniformity resides. For a given orientation of the particle, $A_{\rm vv}(\psi)$ results from individual dipole contributions. Indeed, by noting that $z_{y,i} = a_{y,i} + ib_{y,i}$ where $a_{y,i}$ and $b_{y,i}$ are real values, we can define via Eq. (9) individual-dipole corrections to

RDG as

$$A_{\mathrm{vv},i}(\psi) = \underbrace{a_{y,i}^2 + b_{y,i}^2}_{\text{magnitude}} - \underbrace{\left[(a_{y,i} - \overline{a_{y,i}})^2 + (b_{y,i} - \overline{b_{y,i}})^2\right]}_{\text{dispersion}}. \tag{11}$$

This equation ensures that $A = \overline{A_{\mathrm{vv},i}(\psi)}$. The local contribution of the correction to RDG, meaning for the volume element at $\mathbf{r}_i$, is thus related to the magnitude of the associated phasor minus a dispersion term for that phasor. Figure 6 displays cross-sectional plots through an isolated sphere, Fig. 6(a) and (b), a bisphere in horizontal orientation in Fig. 6(c) and (d), and a bisphere in vertical orientation in Fig. 6(e) and (f). The left column here, plots (a), (c) and (e), show the local contributions to the RDG correction, $A_{\mathrm{vv},i}(\psi)$, while the right column, plots (b), (d) and (f), show the dispersion term of Eq. 11. Note that the discretization of the bisphere volume over the cubic lattice in the DDA results in a misrepresentation of the true particle-shape across the particle surface. Indeed, some degree of a surface effect is seen in Fig. 6. These "shape errors" are well known in DDA studies, e.g., see [22], and there is a possibility that such errors could generate erroneous phasor calculations. In Appendix B, we investigate this possibility and find that for the conditions considered in this study, shape errors are negligible.

For an isolated sphere, Fig. 6(a), the spatial variation of the internal field causes a variation of $A_{\mathrm{vv},i}(\psi)$. The correction is larger across the surface exposed to the oncoming incident wave and decreases with distance into the particle along the x-axis. The gradient of $A_{vv,i}(\psi)$ decreases with an increasing $E(m)$ as shown in Fig. E.11, which reduces the overall correction A. The dispersion term, Fig. 6(a), on the other hand is negligible. For the bisphere, Fig. 6(c), (d), (e), and (f), both $A_{\mathrm{vv},i}$ and the dispersion term exhibit strong gradients at the location of sharpest curvature of the shape, i.e., at the intersections of the spheres. This effect is reminiscent of the field enhancements found in the vicinity of sharp edges at the intersection of perfect conductors [33]. Of course, these spheres are not perfect conductors and the behavior of the field near the sphere-sphere intersection is an area for further study. Some work related to this situation is available, showing evidence for field enhancement here, see [34].

Figure 6 also explains why the dispersion is larger for the bisphere than an isolated sphere; compare plot (b) to plots (d) and (f). The cusp-like feature of the bisphere cause

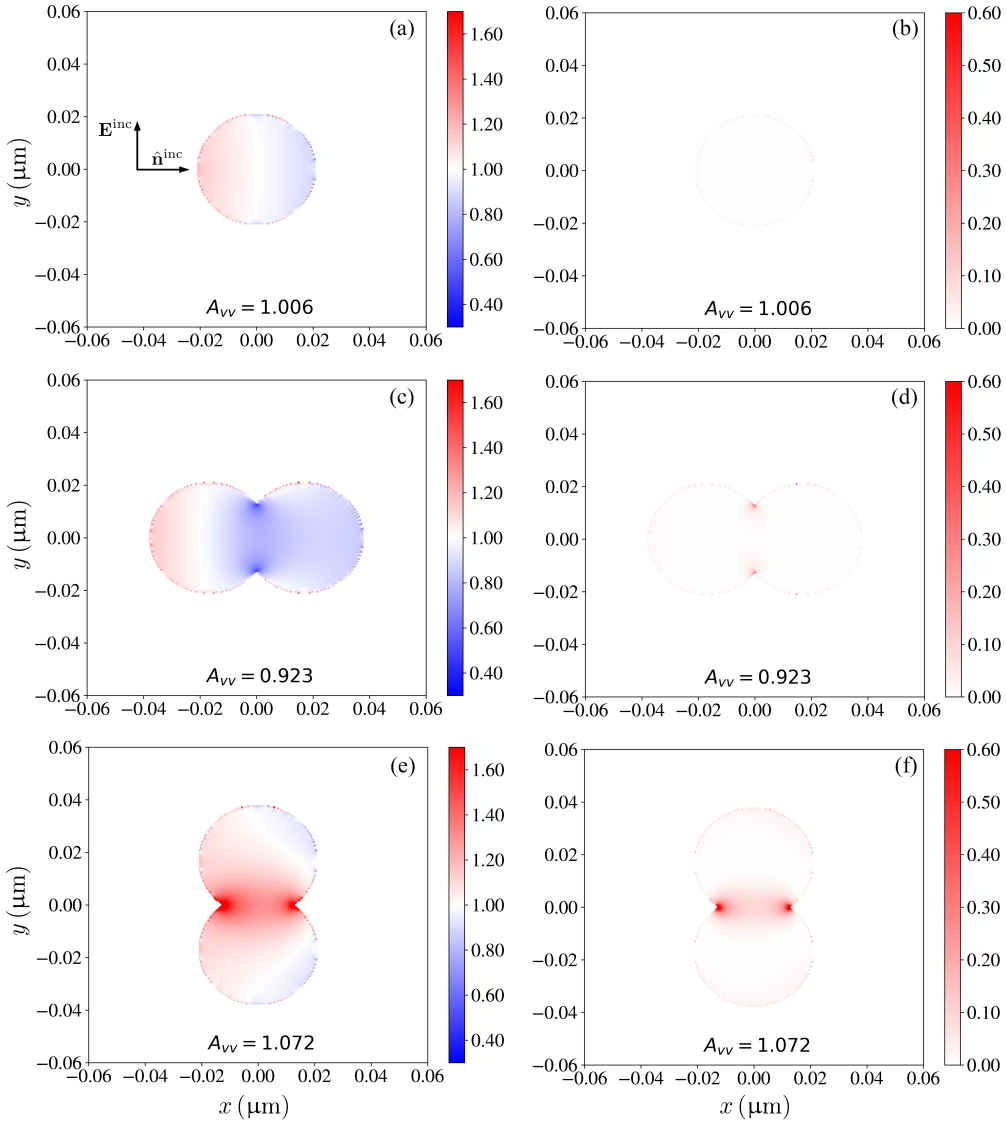

Figure 6: Representation of the local correction to RDG in different particles. Cross-sectional plots are shown for and isolated sphere in the first row, a horizontal- or vertical-oriented bisphere with $d_{ij}/2a = 0.8$ in the second and third rows, respectively. The first column plots $A_{\mathrm{vv},i}$ while the second column plots the dispersion term of $A_{\mathrm{vv},i}$ of Eq. (11). The refractive index is $m = 1.17 + 0.77i$, corresponding to $E(m) = 0.5$ and $F(m) = 0.3$, $\lambda = 532\,\mathrm{nm}$, and the component spheres of the bisphere have radii $a = 21.1\,\mathrm{nm}$. The incident wave is polarized vertically, along the y-axis, and propagates along the x-axis.

larger contributions to the dispersion term for both particle orientations, see plots (d) and (f). Observe that in these regions in the particle exhibit an opposite trend in terms of local correction to RDG $A_{\mathrm{vv},i}$, i.e., plots (c) and (e). The contact between spheres contributes an overall correction of $A < 1$ for the horizontal orientation and $A > 1$ vertical where the volume elements in the neighborhood of this contact produce the largest dispersion in the phasor plot.

The analysis confirms what is expected; that the orientation of the bisphere impacts the scattered intensity in the forward direction [35]. The internal distribution of the correction to the RDG approximation uncovers causes for the large phasor-dispersion in Figs. 4 and 5. Sharp curvatures produce large gradients of the electric field, and thus, significant over- or under-estimation relative to the RDG depending on the particle orientation. For all λ considered, Fig.5), horizontal alignment favors $A < 1$ and vertical alignment $A > 1$.

3.4. RDG correction to the absorption cross section

Drain's expression [21] can be used to express the particle's absorption cross section C^{abs} in terms of the internal electric field, see Appendix F. Consequently, it is also possible to formulate a correction factor for C^{abs} in terms of phasors given vertically polarized incident light, namely

$$h_{\mathrm{v}}(\psi) = \frac{C^{\mathrm{abs}}_{\mathrm{v}}}{C^{\mathrm{abs}}_{\mathrm{RDG,v}}} = \overline{|z_{x,i}|^2} + \overline{|z_{y,i}|^2} + \overline{|z_{z,i}|^2}, \tag{12}$$

where x, y, and z denote the components of the internal electric field. Similar to A_{vv}, the absorption correction h_{v} depends on the particle orientation relative to the incident field. Equation (12) shows that both non-uniformity of the internal field as well as the particle geometry will affect the correction value. After averaging over the particle orientations one obtains $h = \langle h_v(\psi) \rangle$.

The three phasor-components of Eq. (12) contributing to h are shown in Fig. 7 for a horizontally and vertically oriented bisphere. We see here that the $\overline{|z_{x,i}|^2}$ and $\overline{|z_{z,i}|^2}$ components are negligible compared to $\overline{|z_{y,i}|^2}$. Notice that changes in h are driven by exactly the same phenomena as those in A which are also based on the $z_{y,i}$ phasors. Indeed, it is shown that $h_{\mathrm{v}}(\psi) \approx \overline{|z_{y,i}|^2}$ corresponds to the addition of $A_{\mathrm{vv},i}$ and the dispersion term, Eq. 11. Similarly, h corresponds to the sum of the results reported in each row of Fig. 6. These results

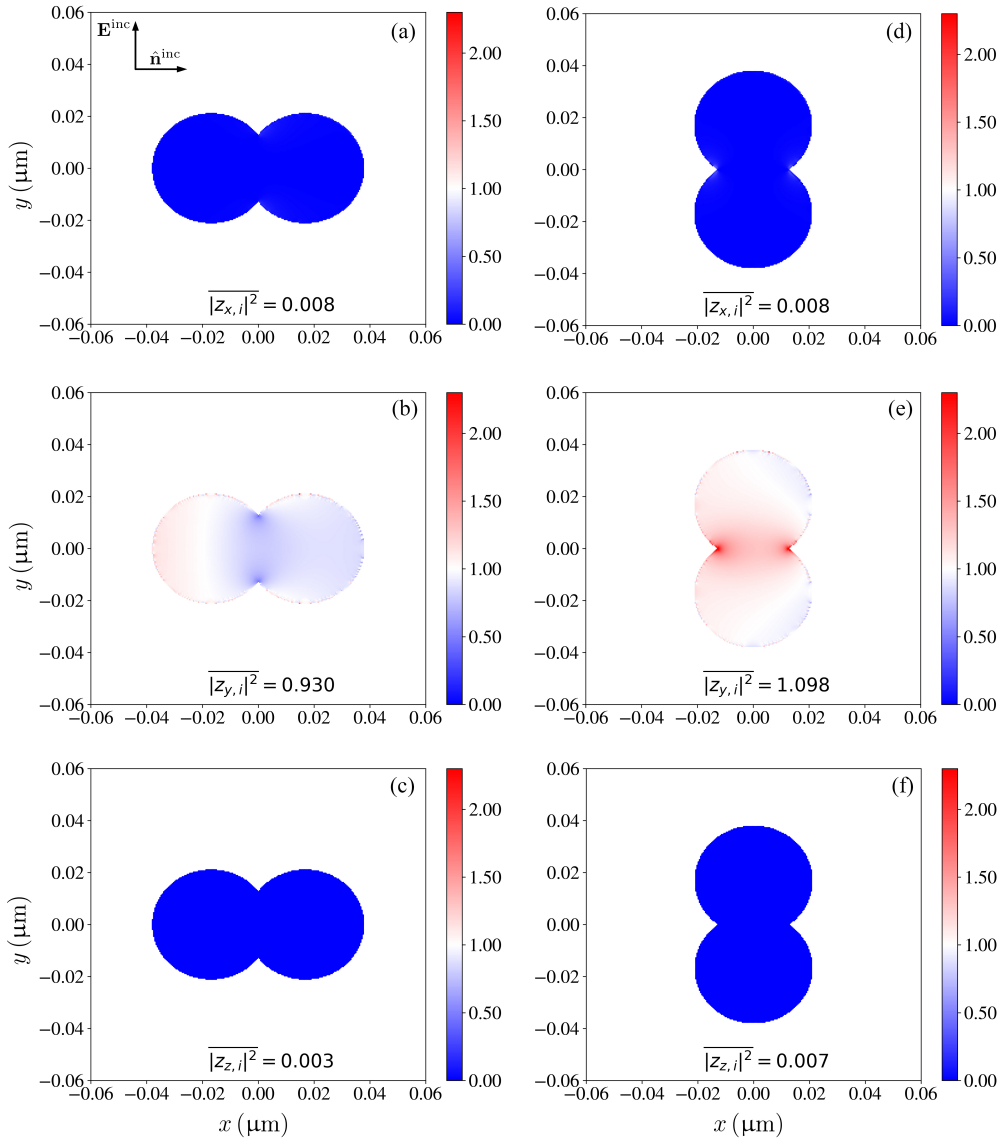

Figure 7: Local correction to the RDG absorption cross-section, h, for a horizontally or vertically oriented bisphere with $d_{ij}/2a = 0.8$, left and right column, respectively. Each row shows $\overline{|z_{x,i}|^2}$, $\overline{|z_{y,i}|^2}$, or $\overline{|z_{z,i}|^2}$ in a cross-section through the bisphere. The refractive index is $m = 1.17 + 0.77i$, corresponding to $E(m) = 0.5$ and $F(m) = 0.3$, $\lambda = 532nm$, and the component sphere radii are $a = 21.1\,\mathrm{nm}$. The incident wave is polarized vertically along the y-axis and propagates along the x-axis.

explain the strong correlation between A and h reported in Yon et al. [10, 11, 12, 14], Liu et al. [13] and Sorensen et al. [15]. Consequently, the overall understanding of phenomenon impacting A described in previous sections stays valid for h.

4. Conclusion

The objective of this work is to enhance the domain of applicability for the RDG approximation so that more accurate optical characterization of nano-particle aerosols and colloids is possible. The absorption and scattering cross-sections provided by the RDG approximation can be inaccurate if $x_{\mathrm{p}} \gg 1$, or $|m-1| > 1$, and if the nano-particles are not spherical and present a certain degree of overlapping. Indeed, if the deviation between the RDG approximation and exact scattering-calculations was already possible based on DDA or T-Matrix approaches, an understanding for the exact role played by size, refractive index, and morphology were less obvious.

Here, we consider a bisphere particle and examine the deviation of the RDG approximation from the exact scattering-calculations through the analysis of the internal electric field using a phasor approach. This phasor analysis clearly indicates that non-uniformity of the field caused by electromagnetic coupling is the origin of the deviation. The coupling between the spheres is limited at short range (no coupling for spheres that are more than two diameters apart). Moreover, the reinterpretation of the electric field in terms of RDG correction maps is proposed for forward scattering and for the absorption cross-sections. It appears that, according to the particle orientation relative to the incident wave, RDG can overestimate or underestimate the scattering and absorption efficiency. The underestimation is moderate in particular if the absorption function $E(m)$ is increased or if the wavelength is decreased, which is due to an increase of the phase shift of the internal electric field. In contrast, increasing the size parameter will result in RDG overestimating the cross-sections. The sharp curvatures occurring at the location of the bisphere interpenetration enhances the electromagnetic coupling which leads to higher deviations of the corrections to bring to RDG. Our study also explains the previously observed strong relationship between correction factors in RDG applied to soot fractal-aggregates for forward scattering and absorption.

This study shows the utility and effectiveness of phasor analysis and motivates its further

application. For example, a logical next-step would be to extend the study beyond a bisphere to an ensemble of N spheres with an arrangement that obeys the fractal-scaling law. Such work may ultimately reveal a complete formulation to correct the RDG approximation for the purpose of efficiently modeling absorption and scattering by soot fractal aggregates; a problem of importance, e.g., in atmospheric science.

Acknowledgments

This work was financed by ANR ASTORIA (N° ANR-18-CE05-0015). We also thank the CRIANN numerical resources supported by the Normandy region. MB acknowledges support from the National Science Foundation, awards 1453987 and 1665456, and the U.S. Air Force Office of Scientific Research award FA9550-19-1-0078.

Appendix A. Applicability of the DDA

Fig. A.8 shows the refractive index dependence of the DDA criterion $|m|kd$ for a fixed interdipolar distance $d = 1.77$ nm and $\lambda = 532$ nm as a function of $F(m)$ and $E(m)$. The main advantage of the DDA is that it is limited only by the interdipolar distance d through the $|m|kd$ criterion. If accurate calculations are desired, numerical study [36] indicates that $|m|kd < 0.5$ should be used. As can be seen, the criteria is very well respected even for the highest values of $|m|$ ($|m|kd = 0.066$). However, the criterion is calculated for $\lambda = 532$ nm while in Fig. 5 reports a wavelength dependence. For this figure, at $\lambda = 266$ nm (which is the most critical wavelength), the criterion is still respected ($|m|kd = 0.059$) due to the chosen optical index.

Appendix B. Dipolar density effect

Figure B.9 shows the effect of the DDA dipole-density on the slices of $A_{\mathrm{vv},i}$ for a vertically oriented bisphere with $d_{ij}/2a = 0.8$ and $m = 1.17 + 0.77i$. Plot (a) is a result of DDA computation based on 14000 dipoles for the bisphere whereas plots (b) and (c) correspond repsectively to 3 and 64 times the value in plot (a). As can be seen, an edge effect resulting from the cubic discretization of the bisphere shape always exist but has negligible effect on the

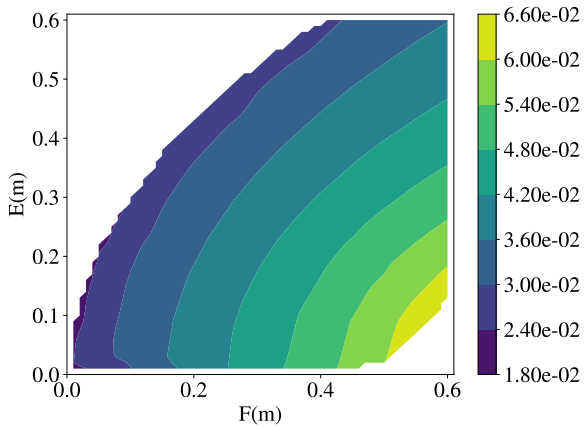

Figure A.8: Evolution of the DDA citerion $|m|kd$ as a function of the refractive index m for a fixed interdipolar distance $d = 1.77$nm and $\lambda = 532$nm.

524 determination of the spatially averaged A_{vv}, indicating that the mean phasor is well-defined even for the smallest dipole density used.

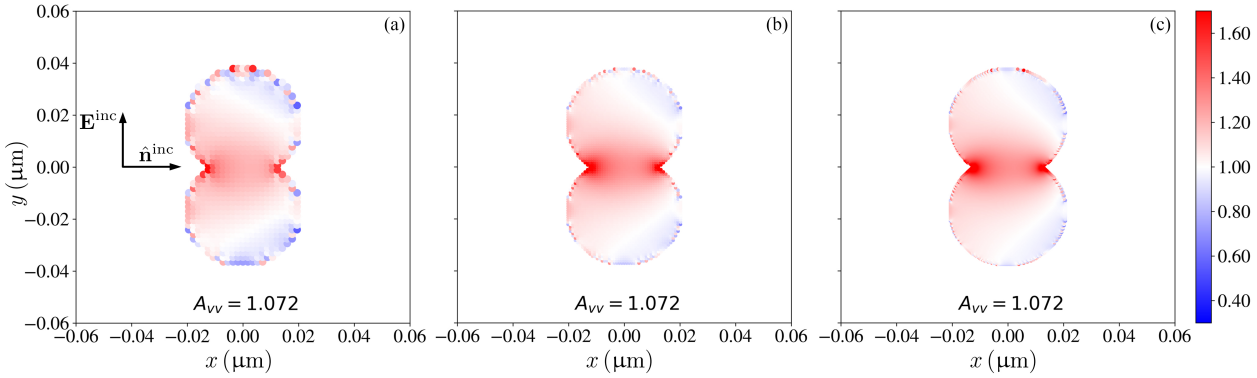

Figure B.9: Effect of the dipole density (number of dipole per volume unit, related to the dipole inter-distance d) on the spatial representation of the correction to bring to RDG forward scattering into agreement with DDA calculations for the vertical-vertical polarization configuration. The wavelength is 532nm and the monomer radius is $a = 21.1$ nm. The incident wave is polarized vertically, along the y-axis, and propagates along the x-axis.

Appendix C. Volume integral equation

Following [25, 37], the scattered electric field $\mathbf{E}^{\rm sca}$ at an observation point $\mathbf{r}$ in a particle's far-field zone is related to the internal field $\mathbf{E}^{\rm int}$ via the volume integral equation (VIE) as

$$\mathbf{E}^{\rm sca}(\mathbf{r}) = \frac{k^2}{4\pi}\frac{\exp(ikr)}{r}(m^2-1)\left(\overleftrightarrow{\mathbf{I}} - \hat{\mathbf{r}}\otimes\hat{\mathbf{r}}\right)\cdot\int_V \mathbf{E}^{\rm int}(\mathbf{r}')\exp(-ik\hat{\mathbf{r}}\cdot\mathbf{r}')\,{\rm d}V', \tag{C.1}$$

where $\overleftrightarrow{\mathbf{I}}$ is the Cartesian identity dyadic and $\hat{\mathbf{r}}\otimes\hat{\mathbf{r}}$ is the dyadic formed by the direct product of $\hat{\mathbf{r}}$ with itself [33, 37]. A useful appendix of dyadic analysis can be found in [38]. In Eq. (C.1), the particle's refractive index m is uniform in the particle volume V otherwise the (m^2-1) must be brought into the integral. Using Cartesian coordinates where $\mathbf{r} = r_x\hat{\mathbf{x}} + r_y\hat{\mathbf{y}} + r_z\hat{\mathbf{z}} = (r_x, r_y, r_z)^{\rm T}$, this product is given by

$$\hat{\mathbf{r}}\otimes\hat{\mathbf{r}} = \frac{1}{r^2}\begin{pmatrix} r_xr_x & r_xr_y & r_xr_z \\ r_yr_x & r_yr_y & r_yr_z \\ r_zr_x & r_zr_y & r_zr_z \end{pmatrix}. \tag{C.2}$$

In the far-field zone, the scattered field is represented by an outward propagating spherical wave modified by a scattering amplitude $\mathbf{E}_1^{\rm sca}$ [26]

$$\mathbf{E}^{\rm sca}(\mathbf{r}) = \frac{\exp(ikr)}{r}\mathbf{E}_1^{\rm sca}(\hat{\mathbf{r}}). \tag{C.3}$$

where the wave is transverse, i.e., $\hat{\mathbf{r}}\cdot\mathbf{E}_1^{\rm sca}(\hat{\mathbf{r}}) = 0$. Equation (C.3) shows that $\mathbf{E}_1^{\rm sca}$ depends on the direction $\hat{\mathbf{r}}$ but not the distance r to the observation point $\mathbf{r}$. Moreover, the scattered wave is transverse, $\hat{\mathbf{r}}\cdot\mathbf{E}^{\rm sca}$ and the scattered magnetic field is given by

$$\mathbf{B}^{\rm sca}(\mathbf{r}) = \frac{\exp(ikr)}{cr}\hat{\mathbf{r}}\times\mathbf{E}_1^{\rm sca}(\hat{\mathbf{r}}), \tag{C.4}$$

where $c = \omega/k$ is the speed of light.

Now consider the behavior of the dyadic term $(\overleftrightarrow{\mathbf{I}} - \hat{\mathbf{r}}\otimes\hat{\mathbf{r}})$ acting on the integral in Eq. (C.1). In the forward-scattering direction $\hat{\mathbf{r}} = \hat{\mathbf{n}}^{\rm inc} = \hat{\mathbf{x}}$ and using Eq. (C.2) this dyadic becomes

$$\overleftrightarrow{\mathbf{I}} - \hat{\mathbf{n}}^{\rm inc}\otimes\hat{\mathbf{n}}^{\rm inc} = \begin{pmatrix} 1 & 0 & 0 \\ 0 & 1 & 0 \\ 0 & 0 & 1 \end{pmatrix} - \begin{pmatrix} 1 & 0 & 0 \\ 0 & 0 & 0 \\ 0 & 0 & 0 \end{pmatrix} = \begin{pmatrix} 0 & 0 & 0 \\ 0 & 1 & 0 \\ 0 & 0 & 1 \end{pmatrix} \tag{C.5}$$

such that for an arbitrary vector $\mathbf{A}$, $(\overleftrightarrow{\mathbf{I}} - \hat{\mathbf{n}}^{\text{inc}} \otimes \hat{\mathbf{n}}^{\text{inc}}) \cdot \mathbf{A} = A_y \hat{\mathbf{y}} + A_z \hat{\mathbf{z}}$. Applying this result to Eq. (C.1) shows that the forward-scattered electric field is given by

$$\mathbf{E}^{\text{sca}}(x\hat{\mathbf{x}}) = \frac{k^2}{4\pi} \frac{\exp(ikx)}{x} (m^2 - 1) \int_V \left[E_y^{\text{int}}(\mathbf{r}') \hat{\mathbf{y}} + E_z^{\text{int}}(\mathbf{r}') \hat{\mathbf{z}} \right] \exp(-ikx') \, \mathrm{d}V', \tag{C.6}$$

which via Eq. (C.3) leads to the forward-scattering amplitude

$$\mathbf{E}_1^{\text{sca}}(\hat{\mathbf{x}}) = \frac{k^2}{4\pi} (m^2 - 1) \int_V \left[E_y^{\text{int}}(\mathbf{r}') \hat{\mathbf{y}} + E_z^{\text{int}}(\mathbf{r}') \hat{\mathbf{z}} \right] \exp(-ikx') \, \mathrm{d}V'. \tag{C.7}$$

Finally, noting that the study is restricted to forward scattering resolved along the vertical polarization direction only, i.e., along the polarization direction of the incident wave, Eq. (4), we retain only the y-component in Eq. (C.7) giving

$$\mathbf{E}_{1,\text{vv}}^{\text{sca}}(\hat{\mathbf{x}}) = \hat{\mathbf{y}} \frac{k^2}{4\pi} (m^2 - 1) \int_V E_y^{\text{int}}(\mathbf{r}') \exp(-ikx') \, \mathrm{d}V', \tag{C.8}$$

which is equivalent to Eq. (5) when Eq. (5) is evaluated at $\hat{\mathbf{r}} = \hat{\mathbf{n}}^{\text{inc}}$.

We note that for an isolated sphere illuminated by the incident wave of Eq. (4), the contribution of E_z^{int} to $\mathbf{E}^{\text{sca}}$ will cancel out in the integral in Eq. (C.7) provided that $\mathbf{r}$ resides in the horizontal scattering plane, the x-z plane, at a fixed distance r. In short, the reason for this is that the internal field in a sphere exhibits several planes of reflection symmetry, which in this case are the x-y (vertical) and x-z (horizontal) planes. Upon reflection of a point $\mathbf{r}'$ in the sphere about the horizontal plane, $E_z^{\text{int}}(\mathbf{r}')$ changes sign while $E_y^{\text{int}}(\mathbf{r}')$ does not [18]. In other words, for an isolated sphere with r constrained as described, $\mathbf{E}_1^{\text{sca}} = \mathbf{E}_{1,\text{vv}}^{\text{sca}}$ and the polarization state of the incident wave is thus preserved upon scattering.

Even the bisphere will exhibit the same reflection symmetry of its internal field when illuminated by Eq. (4) and its axis of rotation is parallel to $\hat{\mathbf{n}}^{\text{inc}}$. If, again, $\mathbf{r}$ is constrained to the horizontal plane at fixed distance r, only the E_y^{int} need be retained in Eq. (C.7) and the polarization state of the scattered wave will be the same as the incident wave. However, if the bisphere is rotated such that its axis of rotation is not parallel to $\hat{\mathbf{n}}^{\text{inc}}$, this reflection symmetry is spoiled and, in general, $\mathbf{E}_1^{\text{sca}} \neq \mathbf{E}_{1,\text{vv}}^{\text{sca}}$ and both internal-field components in Eq. (C.7) must be retained. In Sec. 2, we do not retain the E_z^{int} in Eq. (C.7) despite considering the average scattering from a bisphere in 400 isotropically distributed orientations. The reason for this is because we specifically want to examine the vertically-scattered light so as to best compare to the RDG approximation where $\mathbf{E}^{\text{int}}$ has only one component given by Eq. (10).

Appendix D. Forward-scattering correction

Fig. D.10 shows the refractive index dependence of the forward-scattering correction A_{vv} for an isolated sphere of radius $a = 21.1\,\text{nm}$ as a function of n and κ where $m = n + i\kappa$. The symbols in the plot correspond to the various values for m used in Fig. 2. Similar to the behavior seen in Fig. D.10, Sorensen et al.[15] observe that increasing n will increase A_{vv} and decreasing κ will decrease A_{vv}. However, we see here that the κ has a comparatively weak impact on A_{vv}, suggesting that the correction factor is dominated by n. It is this observation that motivates us to examine the behavior of A_{vv} as a function of $F(m)$ and $E(m)$ in Fig. 2(c) rather than as a function of n and κ.

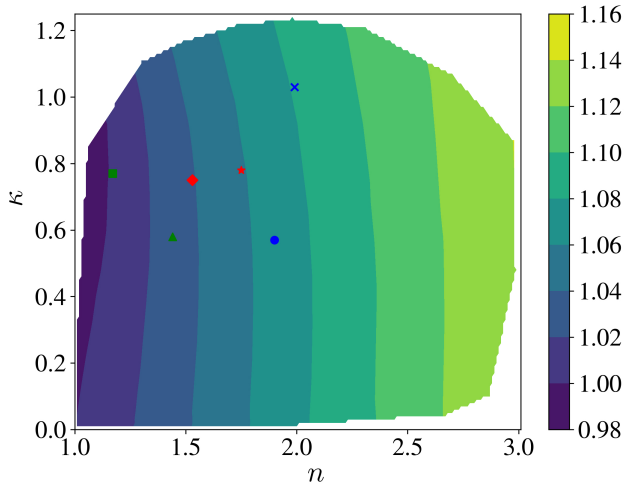

Figure D.10: Refractive index m dependence of the RDG correction factor A_{vv} for an isolated sphere with radius $a = 21.1\,\text{nm}$ where the symbols correspond to those in Fig. 2.

Appendix E. Spatial representation of the correction to RDG

Figure E.11 reports different cross-sectional views of an isolated sphere of radius $a = 21.1\,\text{nm}$ for a variable $E(m)$ and fixed $F(m) = 0.30$, where the first column [plots (a), (c), and (d)] correspond to the local contributions to the RDG correction (A_{vv}, and the second column [plots (b), (d), and (f)] correspond to the dispersion term, cf. Eq. (11). The first row is for a refractive index of $m = 1.17 + 0.77i$ corresponding to $E(m) = 0.5$, the second row for $m = 1.53 + 0.75i$ corresponding to $E(m) = 0.35$, and the last last row for $m = 1.90 + 0.57i$

corresponding to $E(m) = 0.20$. The incoming light is polarized vertically (y direction), propagates along the x direction with a wavelength of $\lambda = 532nm$.

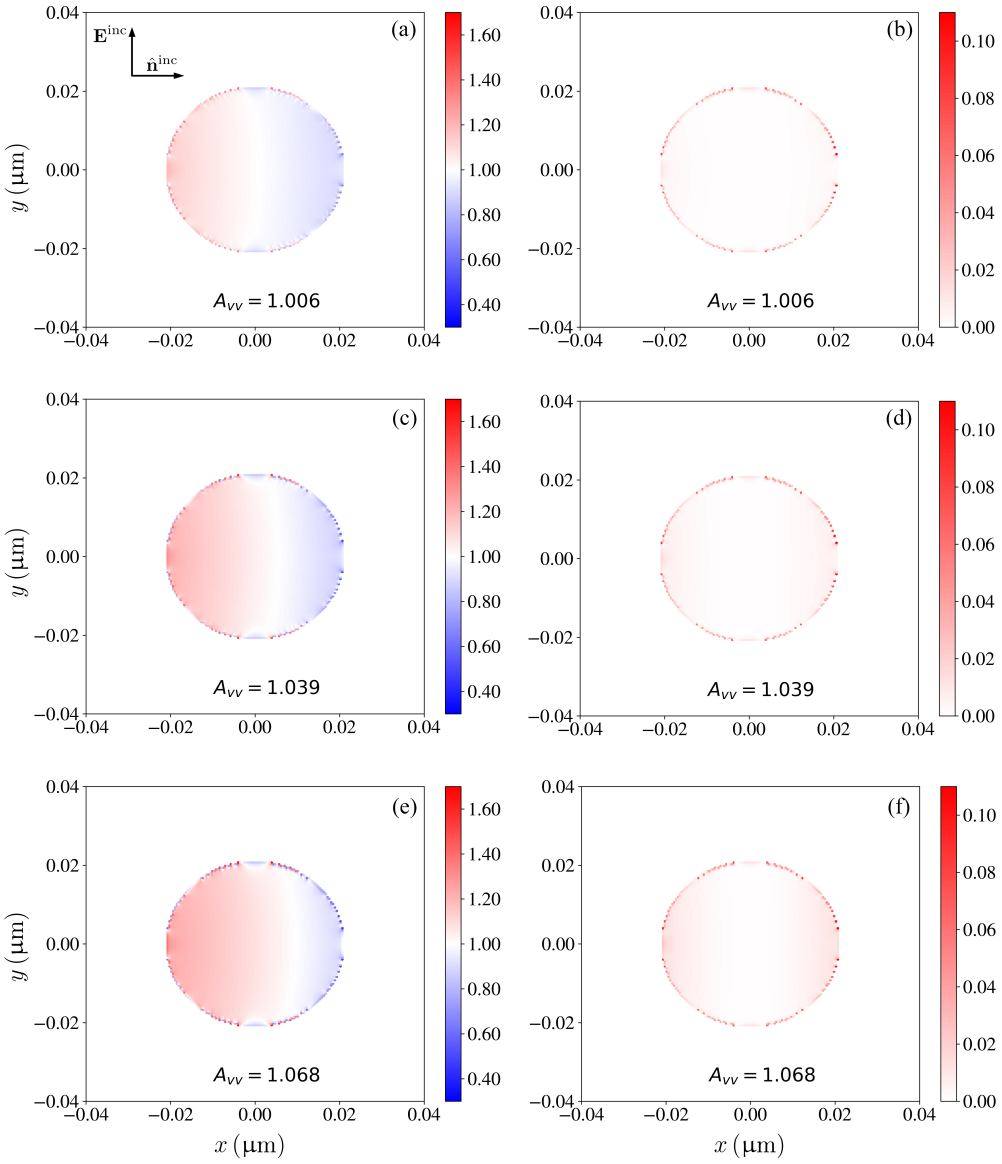

Figure E.11: Representation of the local correction to RDG in cuts of the material for different $E(m)$ of an isolated sphere where $F(m) = 0.30$. First column corresponds to $A_{\mathrm{vv},i}(\psi)$ (local correction to RDG for a given orientation) and second one represents the dispersion contribution of $A_{\mathrm{vv},i}(\psi)$ to $A_{\mathrm{vv}}(\psi)$. Plots (a)-(b) corresponds to a refractive index of $m = 1.17 + 0.77i$, corresponding to $E(m) = 0.5$, plots (c)-(d) have $m = 1.53 + 0.75i$ corresponding to $E(m) = 0.35$, and plots (e)-(f) have $m = 1.90 + 0.57i$ corresponding to $E(m) = 0.20$. The wavelength is 532nm and the monomer radius is $a = 21.1$ nm. The incoming light is polarized vertically (y direction) and propagates along the x direction.

Appendix F. Phasor definition of deviation ratios

We next consider the derivation of Eq. (9) within the framework of the phasor description for forward scattering. The intensity of the scattered wave in the vertical-vertical polarization configuration $I_{\mathrm{vv}}^{\mathrm{sca}}$ is defined in terms of the time-averaged Poynting vector of that wave $\langle \mathbf{S}^{\mathrm{sca}} \rangle_t$ and is related to the differential scattering cross section as [37]

$$\frac{\mathrm{d}C_{\mathrm{vv}}^{\mathrm{sca}}}{\mathrm{d}\Omega}(\hat{\mathbf{r}}) = \frac{r^2 I_{\mathrm{vv}}^{\mathrm{sca}}(\mathbf{r})}{I^{\mathrm{inc}}} = \frac{r^2}{I^{\mathrm{inc}}} \left| \langle \mathbf{S}^{\mathrm{sca}}(\mathbf{r}) \rangle_t \right|, \tag{F.1}$$

where $I^{\mathrm{inc}} = (1/2)\sqrt{\epsilon_{\mathrm{o}}/\mu_{\mathrm{o}}} E_{\mathrm{o}}^2$, ϵ_{o} is the permittivity of free space, μ_{o} is the permeability of free space, i.e., $1/(\epsilon_{\mathrm{o}}\mu_{\mathrm{o}}) = c^2$, and it is understood that only the vertical component of the scattered field is used as indicated in Eq. (F.2) below. The Poynting vector in Eq. (F.1) can be simplified using Eqs. (C.3) and (C.4) as

$$\langle \mathbf{S}^{\mathrm{sca}}(\mathbf{r}) \rangle_t = \frac{1}{2\mu_{\mathrm{o}}} \mathrm{Re}\left\{ \mathbf{E}^{\mathrm{sca}}(\mathbf{r}) \times [\mathbf{B}^{\mathrm{sca}}(\mathbf{r})]^* \right\} = \frac{1}{2r^2} \sqrt{\frac{\epsilon_{\mathrm{o}}}{\mu_{\mathrm{o}}}} \left| \mathbf{E}_1^{\mathrm{sca}}(\hat{\mathbf{r}}) \cdot \hat{\mathbf{y}} \right|^2 \hat{\mathbf{r}}, \tag{F.2}$$

Then, using Eq. (F.1) with Eq. (6) and selecting the forward-scattering direction we find that

$$\frac{\mathrm{d}C_{\mathrm{vv}}^{\mathrm{sca}}}{\mathrm{d}\Omega}(\hat{\mathbf{n}}^{\mathrm{inc}}) = \frac{\left| \mathbf{E}_1^{\mathrm{sca}}(\hat{\mathbf{n}}^{\mathrm{inc}}) \cdot \hat{\mathbf{y}} \right|^2}{E_{\mathrm{o}}^2} = \left(\frac{3k^2}{4\pi} \right)^2 F(m) \left| \sum_{i=1}^{N} z_{y,i}(\hat{\mathbf{n}}^{\mathrm{inc}}) \, \Delta V \right|^2. \tag{F.3}$$

Meanwhile, the analog to Eq. (F.3) in the RDG approximation is given by Eq. (5) with E_y^{int} replaced by Eq. (10) using Eq. (4). Then, for this analog, again using Eq. (F.1) with Eq. (6) and selecting the forward-scattering direction, we find that

$$\frac{\mathrm{d}C_{\mathrm{RDG}}^{\mathrm{sca}}}{\mathrm{d}\Omega}(\hat{\mathbf{n}}^{\mathrm{inc}}) = \frac{\left| \mathbf{E}_1^{\mathrm{sca}}(\hat{\mathbf{r}}) \cdot \hat{\mathbf{y}} \right|^2}{E_{\mathrm{o}}^2} = \left(\frac{3k^2}{4\pi} \right)^2 F(m) V^2 \tag{F.4}$$

because $z_{y,i}(\hat{\mathbf{n}}^{\mathrm{inc}}) = 1 + 0i$, and therefore, $\sum_{i=1}^{N} z_{y,i}(\hat{\mathbf{n}}^{\mathrm{inc}}) \, \Delta V = N \Delta V = V$. The ratio of Eqs. (F.3) and (F.4) defines the deviation measure of Eq. (9), i.e.,

$$A_{\mathrm{vv}}(\psi) = \frac{\dfrac{\mathrm{d}C_{\mathrm{vv}}^{\mathrm{sca}}}{\mathrm{d}\Omega}(\hat{\mathbf{n}}^{\mathrm{inc}})}{\dfrac{\mathrm{d}C_{\mathrm{RDG}}^{\mathrm{sca}}}{\mathrm{d}\Omega}(\hat{\mathbf{n}}^{\mathrm{inc}})} = \left| \frac{1}{V} \sum_{i=1}^{N} z_{y,i}(\hat{\mathbf{n}}^{\mathrm{inc}}) \, \Delta V \right|^2 = |\overline{z_{y,i}}|^2. \tag{F.5}$$

In a similar fashion, it is possible to define a deviation measure for the total absorption cross section C^{abs} relative to the RDG approximation for an incident vertically polarized

wave. Using the optical theorem, Draine et al. [21] provide a definition for C^{abs} in terms of the dipole moments $\mathbf{P}_i$ in the DDA as

$$C_{\text{v}}^{\text{abs}} = \frac{4\pi k}{|\mathbf{E}^{\text{inc}}|^2} \sum_{i=1}^{N} \left[\text{Im}\left\{ \mathbf{P}_i \cdot \left(\alpha^{-1}\mathbf{P}_i\right)^* \right\} - \frac{2k^3}{3} \mathbf{P}_i \cdot \mathbf{P}_i^* \right]. \tag{F.6}$$

In Eq. (F.6), $\mathbf{P}_i$ is the complex-valued electric dipole moment associated with a volume element ΔV and α is the polarizability, which is taken as constant throughout the particle volume V in our case. This expression differs from that of Purcell and Pennypacker [20] due to the $(2/3)k^3\mathbf{P}_i \cdot \mathbf{P}_i$ term, which is included to account for radiation reaction. Each dipole is established by an exciting field $\mathbf{E}^{\text{exc}}$ as $\mathbf{P}_i = \alpha \mathbf{E}^{\text{exc}}(\mathbf{r}_i)$ where this field is not the same as the (macroscopic) field $\mathbf{E}^{\text{int}}$ appearing in Eq. (C.1). The exciting field is the field due to the incident wave plus the fields radiated to dipole i from all other dipoles excluding the field of dipole i itself [21]. Yet, Yurkin et al. [22] show that the moments are proportional to the macroscopic internal field as $\mathbf{P}_i = \chi \mathbf{E}^{\text{int}}(\mathbf{r}_i)\Delta V$ where χ is the electric susceptibility given by [39] as $\chi = \frac{1}{4\pi}(m^2 - 1)$. Installing these definitions in Eq. (F.6) and noting that $|\mathbf{E}^{\text{inc}}|^2 = E_{\text{o}}^2$ gives

$$C_{\text{v}}^{\text{abs}} = \frac{k}{4\pi} \frac{|m^2 - 1|^2}{E_{\text{o}}^2} \left[\text{Im}\left\{ \frac{1}{\alpha^*} \right\} - \frac{2k^3}{3} \right] (\Delta V)^2 \sum_{i=1}^{N} \left\{ \mathbf{E}^{\text{int}}(\mathbf{r}_i) \cdot \left[\mathbf{E}^{\text{int}}(\mathbf{r}_i) \right]^* \right\}. \tag{F.7}$$

To express this in terms of phasors, we must generalize Eq. (7) to the case when all vector components of the internal field are considered, i.e., we take

$$z_{\nu,i}(\hat{\mathbf{r}}) = \hat{\mathbf{n}}_\nu \frac{m^2 + 2}{3E_{\text{o}}} E_\nu^{\text{int}}(\mathbf{r}_i) \exp(-ik\hat{\mathbf{r}} \cdot \mathbf{r}_i) \tag{F.8}$$

where $\nu = \{x, y, z\}$ and $\hat{\mathbf{n}}_\nu = \{\hat{\mathbf{x}}, \hat{\mathbf{y}}, \hat{\mathbf{z}}\}$. Then, Eq. (F.8) can be inverted to express the internal field in terms of phasor components as

$$\mathbf{E}^{\text{int}}(\mathbf{r}_i) = \frac{3E_{\text{o}}}{m^2 + 2} \left[z_{x,i}(\hat{\mathbf{r}})\hat{\mathbf{x}} + z_{y,i}(\hat{\mathbf{r}})\hat{\mathbf{y}} + z_{z,i}(\hat{\mathbf{r}})\hat{\mathbf{z}} \right] \exp(ik\hat{\mathbf{r}} \cdot \mathbf{r}_i). \tag{F.9}$$

Note that the field product in Eq. (F.7) will remove the exponential in Eq. (F.9), and thus, we can ignore the exponential in Eq. (F.8). Then, using Eq. (F.9) in Eq. (F.7) gives

$$C_{\text{v}}^{\text{abs}} = \frac{9k}{4\pi} (\Delta V)^2 F(m) \left[\text{Im}\left\{ \frac{1}{\alpha^*} \right\} - \frac{2k^3}{3} \right] \sum_{i=1}^{N} \left[|z_{x,i}|^2 + |z_{y,i}|^2 + |z_{z,i}|^2 \right]. \tag{F.10}$$

As demonstrated, in the RDG regime for a vertically incident light source, $z_{y,i} = 1+i0$ and $z_{x,i} = z_{z,i} = 0$. Also, by replacing α by the Draine [21] expression $\alpha^{CM}[1-\frac{i}{2\pi}(k^3\Delta V)\frac{m^2-1}{m^2+2}]^{-1}$ (α^{CM} : Clausius Mossotti relation) and by assuming that the DDA discreatization is high enough to ensure $k^3\Delta V \to 0$, the term $\frac{i}{2\pi}(k^3\Delta V)\frac{m^2-1}{m^2+2}$ in brackets becomes negligible and we then obtain

$$C_{\mathrm{v,RDG}}^{\mathrm{abs}} = \frac{6k^4}{4\pi} N(\Delta V)^2 F(m) \left[\frac{2\pi}{k^3\Delta V} \mathrm{Im}\left\{ \left(\frac{m^2+2}{m^2-1} \right)^* \right\} - 1 \right] \tag{F.11}$$

Once again, with the assumption that the DDA discretization is high enough to ensure $k^3\Delta V \to 0$, the term -1 in brackets will also be negligible. After simplification of the remaining terms in Eq. (F.11), we obtain the classical expression of the RDG absorption cross section

$$C_{\mathrm{v,RDG}}^{\mathrm{abs}} = \frac{6\pi V}{\lambda} E(m) \tag{F.12}$$

with $E(m)$ given by Eq. (1). Finally, the ratio of Eq. (F.10) with the same equation using $z_{y,i} = 1 + i0$ and $z_{x,i} = z_{z,i} = 0$ gives the deviation measure h_{v} for the absorption cross section

$$h_{\mathrm{v}} = \frac{C_{\mathrm{v}}^{\mathrm{abs}}}{C_{\mathrm{v,RDG}}^{\mathrm{abs}}} = \frac{1}{N} \sum_{i=1}^{N} \left[|z_{x,i}|^2 + |z_{y,i}|^2 + |z_{z,i}|^2 \right], \tag{F.13}$$

which is Eq. (12).

References

[1] G. A. Kelesidis, E. Goudeli, S. E. Pratsinis, Flame synthesis of functional nanostructured materials and devices: Surface growth and aggregation, Proceedings of the Combustion Institute 36 (2017) 29 – 50. URL: http://www.sciencedirect.com/science/article/pii/S1540748916304679. doi:https://doi.org/10.1016/j.proci.2016.08.078.

[2] C. Motzkus, C. Chivas-Joly, E. Guillaume, S. Ducourtieux, L. Saragoza, D. Lesenechal, T. Macé, J.-M. Lopez-Cuesta, C. Longuet, Aerosols emitted by the combustion of polymers containing nanoparticles, Journal of nanoparticle research 14 (2012) 687.

[3] B. Giechaskiel, F. Riccobono, T. Vlachos, P. Mendoza-Villafuerte, R. Suarez-Bertoa, G. Fontaras, P. Bonnel, M. Weiss, Vehicle emission factors of solid nanoparticles in

the laboratory and on the road using portable emission measurement systems (pems), Frontiers in Environmental Science 3 (2015) 82.

[4] C. F. Bohren, D. R. Huffman, Absorption and scattering of light by small particles, John Wiley & Sons, 2008.

[5] J. B. Maughan, C. M. Sorensen, Application of the scaling approach to particles having simple, fundamental shapes, in the rayleigh–debye–gans diffraction limit, Journal of Quantitative Spectroscopy and Radiative Transfer 222-223 (2019) 190 – 195. URL: http://www.sciencedirect.com/science/article/pii/S0022407318305053. doi:https://doi.org/10.1016/j.jqsrt.2018.10.037.

[6] C. Sorensen, Light scattering by fractal aggregates: a review, Aerosol Science & Technology 35 (2001) 648–687.

[7] T. L. Farias, Ü. Ö. Köylü, M. d. G. Carvalho, Range of validity of the rayleigh–debye–gans theory for optics of fractal aggregates, Applied optics 35 (1996) 6560–6567.

[8] R. Ceolato, L. Paulien, J. B. Maughan, C. M. Sorensen, M. J. Berg, Radiative properties of soot fractal superaggregates including backscattering and depolarization, Journal of Quantitative Spectroscopy and Radiative Transfer 247 (2020) 106940. URL: http://www.sciencedirect.com/science/article/pii/S0022407319307939. doi:https://doi.org/10.1016/j.jqsrt.2020.106940.

[9] F. Liu, G. J. Smallwood, Effect of aggregation on the absorption cross-section of fractal soot aggregates and its impact on lii modelling, Journal of Quantitative Spectroscopy and Radiative Transfer 111 (2010) 302 – 308. URL: http://www.sciencedirect.com/science/article/pii/S0022407309002325. doi:https://doi.org/10.1016/j.jqsrt.2009.06.017, eurotherm Seminar No. 83: Computational Thermal Radiation in Participating Media III.

[10] J. Yon, C. Rozé, T. Girasole, A. Coppalle, L. Méès, Extension of rdg-fa for scattering prediction of aggregates of soot taking into account interactions of large monomers, Particle & Particle Systems Characterization 25 (2008) 54–67.

[11] J. Yon, F. Liu, A. Bescond, C. Caumont-Prim, C. Rozé, F.-X. Ouf, A. Coppalle, Effects of multiple scattering on radiative properties of soot fractal aggregates, Journal of Quantitative Spectroscopy and Radiative Transfer 133 (2014) 374–381.

[12] J. Yon, A. Bescond, F. Liu, On the radiative properties of soot aggregates part 1: Necking and overlapping, Journal of Quantitative Spectroscopy and Radiative Transfer 162 (2015) 197–206.

[13] F. Liu, J. Yon, A. Bescond, On the radiative properties of soot aggregates–part 2: Effects of coating, Journal of Quantitative Spectroscopy and Radiative Transfer 172 (2016) 134–145.

[14] J. Yon, F. Liu, J. Morán, A. Fuentes, Impact of the primary particle polydispersity on the radiative properties of soot aggregates, Proceedings of the Combustion Institute 37 (2019) 1151–1159.

[15] C. M. Sorensen, J. Yon, F. Liu, J. Maughan, W. R. Heinson, M. J. Berg, Light scattering and absorption by fractal aggregates including soot, Journal of Quantitative Spectroscopy and Radiative Transfer 217 (2018) 459–473.

[16] G. A. Kelesidis, M. R. Kholghy, J. Zuercher, J. Robertz, M. Allemann, A. Duric, S. E. Pratsinis, Light scattering from nanoparticle agglomerates, Powder Technology 365 (2020) 52 – 59. URL: http://www.sciencedirect.com/science/article/pii/S0032591019300993. doi:https://doi.org/10.1016/j.powtec.2019.02.003, sI: In honor of LS Fan.

[17] M. J. Berg, Power-law patterns in electromagnetic scattering: A selected review and recent progress, Journal of Quantitative Spectroscopy and Radiative Transfer 113 (2012) 2292 – 2309. URL: http://www.sciencedirect.com/science/article/pii/S002240731200266X. doi:https://doi.org/10.1016/j.jqsrt.2012.05.015, electromagnetic and Light Scattering by non-spherical particles XIII.

[18] M. Berg, C. Sorensen, A. Chakrabarti, Reflection symmetry of a sphere's internal field and its consequences on scattering: A microphysical approach, Journal of the

Optical Society of America. A, Optics, image science, and vision 25 (2008) 98–107. doi:10.1364/JOSAA.25.000098.

[19] M. J. Berg, C. M. Sorensen, Internal fields of soot fractal aggregates, J. Opt. Soc. Am. A 30 (2013) 1947–1955. URL: http://josaa.osa.org/abstract.cfm?URI=josaa-30-10-1947. doi:10.1364/JOSAA.30.001947.

[20] E. M. Purcell, C. R. Pennypacker, Scattering and Absorption of Light by Nonspherical Dielectric Grains, apj 186 (1973) 705–714. doi:10.1086/152538.

[21] B. T. Draine, The Discrete-Dipole Approximation and Its Application to Interstellar Graphite Grains, apj 333 (1988) 848. doi:10.1086/166795.

[22] M. A. Yurkin, A. G. Hoekstra, The discrete dipole approximation: An overview and recent developments, jqsrt 106 (2007) 558–589. doi:10.1016/j.jqsrt.2007.01.034. arXiv:0704.0038.

[23] L. Liu, M. I. Mishchenko, Scattering and radiative properties of complex soot and soot-containing aggregate particles, Journal of Quantitative Spectroscopy and Radiative Transfer 106 (2007) 262 – 273. URL: http://www.sciencedirect.com/science/article/pii/S0022407307000350. doi:https://doi.org/10.1016/j.jqsrt.2007.01.020, iX Conference on Electromagnetic and Light Scattering by Non-Spherical Particles.

[24] B. T. Draine, P. J. Flatau, Discrete-dipole approximation for scattering calculations, J. Opt. Soc. Am. A 11 (1994) 1491–1499. URL: http://josaa.osa.org/abstract.cfm?URI=josaa-11-4-1491. doi:10.1364/JOSAA.11.001491.

[25] M. I. Mishchenko, L. D. Travis, A. A. Lacis, Multiple Scattering of Light by Particles: Radiative Transfer and Coherent Backscattering, Cambridge University Press, Cambridge, 2006.

[26] M. I. Mishchenko, Far-field approximation in electromagnetic scattering, Journal of Quantitative Spectroscopy & Radiative Transfer 100 (2006) 268—-276.

[27] M. I. Mishchenko, Poynting–stokes tensor and radiative transfer in discrete random media: The microphysical paradigm, Opt. Ex. 18 (2010) 19770–19791.

[28] A. Brasil, T. L. Farias, M. Carvalho, A recipe for image characterization of fractal-like aggregates, Journal of Aerosol Science 30 (1999) 1379–1389.

[29] F. Ouf, J. Yon, P. Ausset, A. Coppalle, M. Maillé, Influence of sampling and storage protocol on fractal morphology of soot studied by transmission electron microscopy, Aerosol Science and Technology 44 (2010) 1005–1017.

[30] I. Romero, J. Aizpurua, G. W. Bryant, F. J. G. de Abajo, Plasmons in nearly touching metallic nanoparticles: singular response in the limit of touching dimers, Opt. Express 14 (2006) 9988–9999. URL: http://www.opticsexpress.org/abstract.cfm?URI=oe-14-21-9988. doi:10.1364/OE.14.009988.

[31] D. J. Griffiths, Introduction to electrodynamics, Pearson, 2013.

[32] M. I. Mishchenko, Scale invariance rule in electromagnetic scattering, Journal of Quantitative Spectroscopy and Radiative Transfer 101 (2006) 411 – 415. URL: http://www.sciencedirect.com/science/article/pii/S0022407306000598. doi:https://doi.org/10.1016/j.jqsrt.2006.02.047, light in Planetary Atmospheres and Other Particulate Media.

[33] J. D. Jackson, Classical electrodynamics; 2nd ed., Wiley, New York, NY, 1975. URL: https://cds.cern.ch/record/100964.

[34] Z. Wang, Z. Peng, K. Lu, Experimental investigation for field-induced interaction force of two spheres, Appl. Phys. Lett. 82 (2003) 1796–1798.

[35] U. Zywietz, M. Schmidt, A. Evlyukhin, C. Reinhardt, J. Aizpurua, B. Chichkov, Electromagnetic resonances of silicon nanoparticle dimers in the visible, ACS Photonics 2 (2015). doi:10.1021/acsphotonics.5b00105.

[36] B. Draine, J. Goodman, Beyond clausius-mossotti: Wave propagation on a polarizable point lattice and the discrete dipole approximation, Astrophysical Journal 405 (1993)

685–697. doi:10.1086/172396, copyright: Copyright 2018 Elsevier B.V., All rights reserved.

[37] M. I. Mishchenko, Electromagnetic Scattering by Particles and Particle Groups: An Introduction, Cambridge University Press, Cambridge, 2014.

[38] J. G. Van Bladel, Electromagnetic Fields; 2nd ed., Wiley, Hoboken, NJ, 2007.

[39] G. H. Goedecke, S. G. O'Brien, Scattering by irregular inhomogeneous particles via the digitized green's function algorithm, Appl. Opt. 27 (1988) 2431–2438.